8-23-2017

Experimental Study and Modeling of Smart Loss Circulation Materials; Advantages and Promises

Ahmed Khaled Abdelmaksoud Mansour
Louisiana State University and Agricultural and Mechanical College, ahmedkhaledmansour.1993@gmail.com

EXPERIMENTAL STUDY AND MODELING OF SMART LOSS CIRCULATION MATERIALS; ADVANTAGES AND PROMISES

A Thesis

Submitted to the Graduate Faculty of the
Louisiana State University and
Agricultural and Mechanical College
in partial fulfillment of the
requirements for the degree of
Master of Science

in

The Craft & Hawkins Department of Petroleum Engineering

by
Ahmed Khaled Abdelmaksoud Mansour
B.S in Louisiana State University, 2015
December 2017

Acknowledgments

This thesis would have not been possible without several contributions. I would like to thank my advisor, Dr. Arash Dahi Taleghani, for giving me the opportunity to work on such a great project and for guiding me through this work and helping me in the times of need. I am also sincerely appreciative for having Dr. Guoqiang Li and Dr. Andrew K. Wojtanowicz as my committee members. They kept me on track and supplied me with resources and innovative hints to keep my research going.

I would also like to give special thanks to my parents, Dr. Khaled Mansour and Dr. Heba Mohammady, for believing in me, supporting me and pushing me to complete my research. I am grateful to my brother, Mohammed Mansour and my grandmothers, Zeinab and Nadia, for always praying for me and giving me their unconditional love.

I also show great gratitude to all my friends for supporting me during this period. Finally, I would like to thank Allah for guiding me, protecting me and helping me in the hard times.

Table of Contents

Acknowledgments ii

List of Tables v

List of Figures vi

Abstract ix

Chapter 1: Introduction 1
1.1 Background 1
1.2 Motivation 3
1.3 Research Objectives 4

Chapter 2: Theory and Literature Review 6
2.1 Lost Circulation 6
2.2 Lost Circulation Materials Market 9
2.3 LCMs Experimental Testing 10
2.4 Wellbore Strengthening 13
2.5 Understanding and Modeling LCM Performance 16
2.5.1 Wellbore Hoop Stress Enhancement and Strengthening Theories 16
2.5.2 Bridging of Particles in Flow 17
2.5.3 Particle Size Selection Theories for Bridging 19
2.5.4 Fracture Width and Length Modeling 20
2.6 Shape Memory Polymers 21

Chapter 3: Experimental Procedure 28
3.1 Experimental Design 28
3.2 Smart LCMs 30
3.3 Experimental Procedure 30

Chapter 4: Numerical Simulation 33
4.1 Introduction 33
4.2 Discrete Element Methods 33
4.2.1 Governing Equations 34
4.2.2 Heat Transfer Between Particles 35
4.3 Computational Fluid Dynamics 36
4.4 Computational Fluid Dynamics and Discrete Element Methods (CFD-DEM) 36
4.4.1 Particle-Fluid Interaction 37
4.4.2 Particle-Fluid Heat Transfer 38
4.5 Simulation Procedure 38
4.5.1 Simulation Validation 39
4.5.2 Cumulative Fluid Loss 40
4.5.3 Concentration of Particles Required to Seal The Fracture 44
4.5.4 Stress Recovered from Smart LCMs 44

Chapter 5: Results and Discussions 45
5.1 Experimental Results and Discussions 45
5.1.1 Sealing Efficiency Test 45
5.1.2 Fluid Loss and Pressure Buildup Test 47
5.1.3 Strain Expansion Measurement Test 49
5.1.4 Permeability Plugging Test 51
5.1.5 Concentration Required for Sealing 54
5.2 Numerical Simulation Results and Discussions 58
5.2.1 Simulation Validation 58
5.2.2 Cumulative Fluid Loss 61
5.2.3 Concentration of Particles Required to Seal the Fracture 67
5.2.4 Stress Recovery of Smart LCM 70

Chapter 6: Conclusions and Recommendations for Future Work 72

Bibliography 75

Appendix A: Permission to Use Published Papers 81

Appendix B: Experimental Components 83

Vita 85

List of Tables

Table 1.1. Cost of Lost Circulation 1

Table 2.1. Fluid loss classifications 6

Table 3.1. Mud Formulation 30

Table 3.2. Dimensions for discs 32

Table 4.1. Properties of the smart LCMs 40

Table 4.2. Pressure variations in the simulation 42

Table 5.1. Pressure buildup and cumulative fluid loss 46

Table 5.2. Results for the strain measurement test 50

Table 5.3. Test Parameters 52

Table 5.4. Thermal expansion for smart LCM 62

Table 5.5. Cumulative fluid loss for each particle size at different inlet pressures 64

Table 5.6. Cumulative fluid loss for the mixed particle sizes at each pressure 65

Table 5.7. Input parameters for recovered stress 70

List of Figures

Figure 1.1.Smart LCM sealing fracture mouth and providing compressional forces to strengthen the wellbore 2

Figure 2.1. HPHT PPA 12

Figure 2.2. Modified particle plugging apparatus (Al-Saba *et al*, 2014) 13

Figure 2.3. Horizontal stresses acting on the wellbore 14

Figure 2.4. Cold-Programming for Shape Memory Polymers (G. Li, 2014) 22

Figure 2.5. Measured stress of different types of SMPs pre-stressed at different values (Li and Nettles, 2010) 27

Figure 3.1. HPHT PPA with LCM Receiver 28

Figure 3.2. PPA cell schematic 29

Figure 3.3. PPA LCM receiver schematic 29

Figure 3.4. Smart LCM before activation and after activation 30

Figure 3.5. Shear stress versus shear rate for mud. 31

Figure 3.6. Viscosity versus shear rate for mud 31

Figure 3.7. Slot disc and tapered disc 32

Figure 4.1. Steps to complete CFD-DEM simulation 37

Figure 4.2. Tapered disc design for simulation 39

Figure 4.3. New fracture shape for simulation 41

Figure 4.4. Boundary conditions for pressure 42

Figure 4.5. Thermal coefficient above glass acitvation temperature 43

Figure 5.1. Effectively Sealed Slot Disc by the smart LCMs. 46

Figure 5.2. Effectively Sealed Tapered Disc by the Smart LCMs. 47

Figure 5.3. Results for slot disc @ 75 Degrees Celsius 48

Figure 5.4. Results for tapered disc @ 75 Degrees Celsius 48
Figure 5.5. Change of Smart LCM size before and after experiment at 3000 psi 50
Figure 5.6. Change in volume of smart LCM versus pressure 51
Figure 5.7. Results for smart LCMs activated at 80℃ 52
Figure 5.8. Results for the non-expanded LCM at 23℃ 53
Figure 5.9. Results for the expanded LCM at 23℃ 54
Figure 5.10. Different LCMs shapes used. 55
Figure 5.11. Fluid loss versus time for slot disc 55
Figure 5.12. Pressure buildup versus time for slot disc. 56
Figure 5.13. Slot disc sealed at different LCM concentrations. 56
Figure 5.14. Fluid loss versus time for tapered disc. 57
Figure 5.15. Pressure buildup versus time for tapered disc. 58
Figure 5.16 Tapered disc sealed in simulation. 59
Figure 5.17. Concentration of particles comparison. 60
Figure 5.18. Cumulative fluid loss comparison. 60
Figure 5.19. Pressure build-up comparison 61
Figure 5.20. Fluid loss for 2mm particles at 1000 psi 62
Figure 5.21. Temperature of fluid before and after 63
Figure 5.22. Velocity of fluid before and after plugging 64
Figure 5.23. Cumulative fluid loss versus time for the mixed particles at 1000 psi 65
Figure 5.24. Comparison of cumulative fluid losses 66
Figure 5.25. Porosity and packing of mixed particles versus 2mm particles 66
Figure 5.26. Number of 2mm particles required for plugging a fracture at 1000 psi. 67

Figure 5.27. Number of particles required to seal the fracture. 68
Figure 5.28. Mixture of 1.5mm and 2mm particles at 1000 psi. 69
Figure 5.29. Number of mixed particles (1.5mm and 2mm) to seal the fracture. 69
Figure 5.30. Recovery stress of the smart LCMs at 1000 psi 71
Figure 5.31. Recovery stress of smart LCM at all pressures 71
Figure A1. Permission to use ARMA 17-0492 81
Figure A2. Permission to use AADE-17-NTCE 074 82
Figure B1. Permeability plugging apparatus 83
Figure B2. LCM receiver 84

Abstract

Lost circulation occurs when mud or cement is lost to the formation while drilling. Lost circulation has been a huge problem and may cause heavy financial costs in the form of lost rig time, mud fluid and in severe cases, well blowout with serious environmental and safety consequences. Despite extensive advances in the last couple of decades, lost circulation materials used today still have disadvantages such as damaging production zones, plugging drilling tools or failing to seal the fractures. Here, we propose a new class of smart expandable lost circulation material (LCM) to remotely control the expanding force and functionality of injected LCM. The utilized smart LCM is made out of anionic shape memory polymers and becomes activated by formation natural heat; hence it can effectively seal fractures' width without damaging production zones and strengthen the wellbore. The activation temperature of the LCMs can be adjusted based on the formation temperature.

In this work, a series of experiments were conducted using a HPHT permeability-plugging apparatus (PPA) to measure the sealing efficiency of the smart LCMs as a proof of concept. Various slot disc sizes were used to mimic different size fractures in the formation. The API RP 13 B-1&2 have been followed as standard test methods to evaluate fluid loss in water based muds. In addition, a fully coupled CFD-DEM model is developed to further study the effectiveness of different size distribution of smart LCMs and to calculate compressional stresses acting on the wellbore from their expansion. These tests will then allow us to improve the design of the smart LCM and also allow us to see if the smart LCM can be implemented in the field.

Chapter 1: Introduction

1.1 Background

Lost circulation has been a problem since early days of rotary drilling. One of the most important decisions that need to be made in drilling operations is choosing the right type and density of drilling fluids. Drilling fluids are used in drilling operations to provide a pressure overbalance in the bottomhole and prevent the wellbore from collapsing. Drilling fluids are also supposed to be circulated down to the bottomhole and come back to the surface for cutting transport and cooling the bit (White, 1956). However, when lost circulation occurs, drilling fluids are lost and lost circulation materials (LCMs) need to be added to the mud to stop further fluid loss. A lost-circulation incident may have a heavy financial and environmental cost that justifies the price of LCM products to treat the problem. Rig nonproductive time is another financial burden in these incidents (Whitfill and Hemphill, 2003). Table 1.1 shows the costs of lost circulation according to API/Marlin Energy and service companies.

Table 1.1. Cost of Lost Circulation

	Onshore Drilling Operation	Offshore Drilling Operation
Number of days spent to control lost circulation	3	7
Cost per day of the drilling operation ($)	65,000	120,000

It can be seen that controlling a lost circulation incident can take from 3 to 7 days. It becomes more expensive if the lost circulation is on an offshore rig than an onshore rig. It was seen that most lost circulation incidents occur in highly permeable, karsted and naturally fractured

formations (Al-Saba *et al*, 2014). According to Marlin Energy Recourses, 26% of the wells around the world experience such problems. Therefore, a solution to such problems should be found.

In addition, lost circulation leads to the mud levels falling, which can cause the well to be in an underbalance pressure state, and in severe cases a kick or even a blowout may occur (Arshad *et al.*, 2014). Since lost circulation is a very important issue, a lot of research has been made to minimize this problem. Lost circulation materials are materials that seal the fractures and minimize mud loss. In this work, a new smart lost circulation material is introduced to effectively seal fractures and strengthen the wellbore.

The smart LCM in this case is activated via the temperature of the bottomhole and can effectively seal the mouth of the fracture as seen in Figure 1.1 or in some cases at the tip of the fracture.

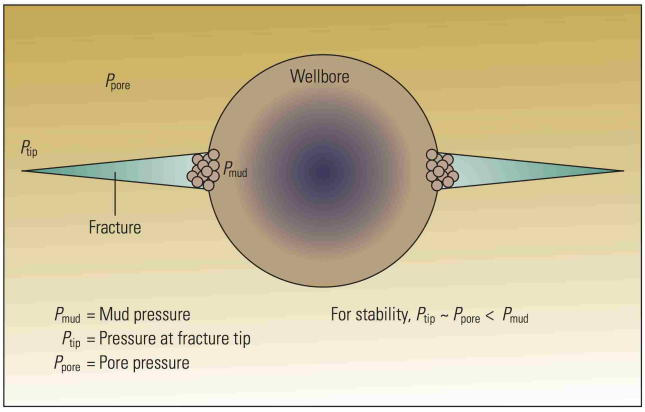

Figure 1.1- Smart LCM sealing fracture mouth and providing compressional forces to strengthen the wellbore

The smart LCM is programmed to be activated at a certain formation temperature based on the lost circulation zone. Since the fracture needs to be sealed properly, our proposed LCM will be made out of anionic shape memory polymers. The bridging and the recovered stress of the shape memory polymers ensure the sealing of the fracture mouth and according to the stress cage

theory it provides compressional forces to strengthen the wellbore (Cook *et al.*, 2012). Therefore, experimental procedures and numerical simulations will be made to test the sealing efficiency of the smart LCM. It is notable that the recovered stress should not be very large to prevent the crack from further propagation. Therefore, a recovered stress ranging from 5-30 MPa is expected and it is reachable with shape memory polymers.

1.2 Motivation

A lot of research and experiments have been made to make sure that LCMs can seal fractures effectively and to minimize loss and non-productive time. However, LCMs still have disadvantages like limited applicability in high-pressure and high-temperature (HPHT) formations or causing damage to producing zones (Brandl *et al.*, 2011). Some LCMs work only for specific formations while fail in others. These LCMs fail because in some formations, the fractures are very large to seal and these LCMs are not designed for big fractures. Therefore, it is important to find a material that can supplement a LCM or be used as an LCM and can seal big fractures and save losses and non-productive time. Drilling engineers have also reported clogging of drilling equipment from LCMs due to their large sizes. They used large size of LCMs because the small ones could not bridge effectively to seal the fractures efficiently.

The smart LCM that is proposed in this thesis has a lot of competitive advantages when compared to the LCMs used today in the field. First, the smart LCM does not only seal the fracture but also provides compressional circumferential stress that acts like a stress cage around the wellbore to strengthen it and to sustain higher mud weight. Second, the developed smart LCM will be programmed through its chemical composition and has the ability to withstand HPHT formations since its shape memory effect is activated through phase transformation by temperature and pressure. Therefore, the smart LCM will be activated at a specific temperature

based on knowing the temperature profile of the wellbore. This will therefore, lower the cost of producing different LCMs for different types of formations. Thirdly, the smart LCM here will be able to work well with all types of muds and it will not dissolve in the mud or fail to change shape while activated. Fourthly, the smart LCM can expand in volume at a certain temperature. Knowing the temperature profile of the wellbore and understanding that the mud temperature is lower than the formation temperature, the equipment used in the field will therefore not be plugged. The LCMs will activate when they leave the bit nozzle and will be able to take the shape of the fracture and seal it. Finally, the smart LCM is acid soluble and therefore, will not cause any damage to production zones. The smart LCM is planned to work with all formations, especially naturally fractured carbonate reservoirs in the Middle East, and depleted zones in the United States such as the formations in the Gulf of Mexico.

1.3 Research Objectives

The research objectives of this thesis are listed below:

1. Conduct experiments to verify the applicability of shape memory polymers as a lost circulation material.
    a) Test the smart LCMs at temperatures below, at and above activation temperature. This will help develop a correlation between temperature and smart LCM sealing.
    b) Test LCM sample with different size distributions and fracture sizes to optimize LCM selection.
    c) Test the expansion of the smart LCM under several different pressures.
2. Simulate LCM bridging and sealing using discrete element methods.
    a) Create a realistic elliptical shape of the fracture through SOLIDWORKS.

b) Model the fracture with LCMs flowing in it through LIGGGHTS (LAMMPS Improved Granular and Granular Heat Transfer Simulations).

c) Measure cumulative fluid losses after inserting the smart LCMs in the fracture using coupling element methods with computational fluid dynamics.

d) Calculate the stress recovery of the smart LCM to verify that it will lead to wellbore strengthening.

e) Validate simulation results with the lab experiment measurements.

f) Measure the concentration of LCMs required to seal the fracture in order to optimize LCM size and distribution.

3. Integrate numerical simulation into lab experiments to improve the design of the SMP as a LCM and therefore, save time and money.

a) Predict the behavior of the sealing efficiency values based on the experimental results and simulations

b) Predict the well performance when the shape memory polymer (SMP) is used as an LCM in a drilling operation that includes fluid loss.

Chapter 2: Theory and Literature Review

This chapter provides a review on what lost circulation is and how it is utilized. An economic analysis section has also been added to help to understand the cost of lost circulation. Experimental and numerical procedures from previous studies are also included for comparison. Finally, a review of what shape memory polymers are and how they are programmed is presented at the end of this chapter.

2.1 Lost Circulation

As mentioned before, lost circulation is the loss of mud or cement to the formation. There are four categories in which lost circulation can be divided into and these are seepage loss, partial loss, severe loss and total loss (Ghalambor *et al.*, 2014). These types of losses are explained with respect to loss rate in Table 2.1 below.

Table 2.1. Fluid loss classifications

Classification	Typical Loss Rate (bbl/hr)
Seepage	<10
Partial	10 to 50
Severe	>50
Total	No Returns

There are a lot of different procedures that can be done in order to minimize or cure lost circulation. According to Cook *et al.* (2012), lost circulation is usually managed through a four-tiered approach. The first tier is usually making sure that the drilling engineer has worked on a predrill simulation and has made the correct calculations concerning mud density. The drilling engineer should also build a geo-mechanical model to understand the type of formation being penetrated and the possibility of any fluid losses. The second tier represents the best selection of drilling fluids. The drilling fluid should have the correct rheological properties that can minimize lost circulation. Properties include viscosity, density and the type of chemicals added to create

the mud. The third tier represents the correct use of wellbore strengthening materials. This tier could also be named as the preventive method and is defined as treatments that are applied before lost circulation occurs in order to prevent mud loss. Wellbore strengthening is defined as a technique to plug and seal induced fractures efficiently while drilling to increase the fracture gradient and widen the mud weight window (Salehi and Nygaard, 2012). Wellbore strengthening materials are mixtures of materials when picked in the correct size, are able to enter the fractures and form a bridge to isolate these fractures from the wellbore (Cook *et al.*, 2012). Finally, the last tier is using lost circulation materials to fix an ongoing lost circulation problem (Cook *et al*, 2012). This tier could be named as the corrective treatment and is defined as the treatments used after mud loss has occurred (Kumar and Savari, 2011).

Lost circulation materials work in a way to ensure that the mud has big enough particles to plug the pores or cracks that mud alone can't seal. This then prevents mud from being lost to the formation (White, 1956). These materials must have special size distributions to ensure efficient fracture sealing (White, 1956). If the size of the particles is too small, the particles will not be able to plug the fracture and will go right through it. Similarly, if the size of the particles is too large, the particles will not be able to enter the fracture and will also not be able to seal it. Therefore, the perfect size of the material's particles is very important so that losses could be treated properly (Jain *et al*, 2013). The type, shape, composition and strength of the materials are also very important when trying to design the most efficient solution for lost circulation (White, 1956). The materials should also be able to adapt to a wide range of environments, temperatures and pressures. The seal formed by the LCMs should be able to withstand mechanical forces that occur due to drilling operations, erosional forces that occur due to fluid flow and hydrodynamic forces that come from swab and surge (Cook *et al*, 2012). LCMs include materials such as

cement, cross-linked cement, chemically activated pills (Bruton *et al*, 2001), lost circulation materials that can change in shape and deform (Whitfill and Wang, 2005), graphite and gunk squeezes (Lecolier *et al*, 2005). The LCMs in the field are usually mixed with the drilling fluid and then pumped to the bottomhole to seal the fractures and prevent an ongoing fluid loss (Al-Saba *et al*, 2014).

Understanding the efficiency of an LCM and evaluating its performance is a critical part when trying to decrease or prevent fluid losses in the bottomhole. Howard *et al*. (1951) first classified the LCMs according to their physical properties. He divided them into four groups being 1) granular 2) fibrous 3) lamellated and 4) dehydratable. White (1956) modified these classifications by adding a new classification where the LCMs are flaky and where also the LCMs can be mixed together to provide better sealing results. Nygaard *et al*. (2014) modified the last two theories and classified LCMs into seven categories being: fibrous, granular, flaky, acid/water soluble, mixture, high fluid loss LCM squeeze, swellable/hydratable LCM combinations and nanoparticles.

1) Fibrous materials - a type of LCM that is slender, long and has low stiffness. It can exist in different sizes and lengths. These materials are very cheap and have proven to efficiently plug fractures. Examples of fibrous materials would be cellulose fibers and saw dust.
2) Granular materials – a type of LCM that is rigid, has high stiffness and crushing resistance. They are often used for wellbore strengthening applications or as preventive treatments. An example of granular materials would be course bentonite.
3) Flaky materials - a type of LCM that has a thin, flat shape with a large surface area. Their stiffness level is similar to fibrous materials and is still capable of sealing the fracture. Examples of flaky materials would be mica and flaked calcium carbonate.

4) Acid or water soluble LCMs – these are LCMs that do not damage the reservoir's permeability. Examples of acid soluble LCMs would be materials that are acid soluble such as calcium carbonate.
5) Mixtures – a combination of different types of lost circulation materials.
6) Swellable/Dehydratable LCMs- these are LCMs that can change in shape. They are usually made out of polymers due to the materials elasticity.
7) Nanoparticles – extremely small and fine particles. Examples of nanoparticles used in the field would be silica, calcium carbonate and iron hydroxide.

2.2 Lost Circulation Materials Market

In terms of economic perspective, it is notable that mud loss to the formation is one of the most costly and undesired encounters in the petroleum industry. It could be induced by drilling or could occur due to the natural fractures of the reservoir itself. It causes a large amount of nonproductive time, which includes all services that support the drilling operation as well as the cost of the rig time. Therefore, since a lost circulation incident costs more than treating it, the industry has been developing new techniques in minimizing lost circulation.

It was estimated that lost circulation alone accounted for US$2- $4 billion annual costs due to lost time (Cook *et al*., 2012). It's not just non-productive time that lost circulation accounts for but uncontrolled loss of fluid can damage the reservoir's formation and have a negative effect on its production potential and therefore, even more future losses (Cook *et al*., 2012). In the Gulf of Mexico, lost circulation, stuck pipe, sloughing shales and wellbore collapse account for 44% of the total non-productive time (Cook *et al*., 2012). Drilling engineers in this area use synthetic-base muds that range from $100 to $200 per barrel and therefore, losing these fluids can be extremely costly. The more the non-productive time, the higher the cost.

According to Industrial Hemp Manufacturing company, the cost of lost circulation materials can be as low as $0.2/lb and reach to over $10/lb. Usually, the expensive LCMs are the plug types that are used as pills while the cheap LCMs are made out of a very cheap material such as sawdust. With cases where the LCMs need to be added continuously to the mud, it is estimated that between 15 lb. to 30 lb. of LCM per barrel of mud should be pumped on every stand, according to Halliburton. The US Energy Information Administration website monitored the costs of drilling from 2002 to 2007. It was reported that the cost per well in 2002 for all wells was about 1 million dollars and by the end of 2007 the cost per well was about 3 and a half million dollars. This means that the cost increased more than triple the amount in just 5 years. The administration also reported the cost of drilling per foot for these 5 years and in 2002 it was $187.46/ft. and almost quadrupled in 2007 to be $574.46/ft. This increase in the cost per foot was caused due to increase in horizontal drilling, lost circulation problems due to fractured formations and other drilling-encountered problems.

The costs of most LCMs used today, as seen above, are very expensive and they could also not work properly in certain formations. This is why a new smart LCM is proposed and it is much cheaper than the LCMs used now. It is almost equivalent to the price of resin which ranges from 0.01$/lb to 0.9$/lb. Having an effective LCM at this cost will save companies even more money specially when the oil prices are about 40$/bbl in 2017.

2.3 LCMs Experimental Testing

There are different experiments that have been made to evaluate the sealing efficiency of LCMs. Kelsey (1981) came up with the first apparatus to test LCM performance. The apparatus used had a maximum temperature of 300 degrees Fahrenheit and a maximum operating pressure of 1000 psi. The LCM was tested with slot discs of various widths that represent fractures in

different types of formations. The efficiency of the LCM was based on the maximum pressure that the seal can withstand in these slot discs.

White (1956) designed criteria to decide which apparatus were perfect for testing the sealing efficiency. The criteria were based on LCM concentrations, volume of fluid loss and pressure build-up of the seal. He also tested the LCMs based on these criteria. The concentration of the LCMs and the fracture sizes was varied to verify LCMs sealing efficiency.

Kumar and Savari (2011) and Savari *et al*. (2013) tested LCMs using the high-pressure high-temperature permeability plugging apparatus ((HPHT-PPA) in Figure 2.1 and a normal permeability plugging apparatus (PPA) in Figure 2.2a. They analyzed the results based on 30 minutes of total fluid loss and the time it takes for the tight seal to form. For the PPA, the pressure is applied from the top and for the HPHT-PPA; pressure is applied from the bottom. These apparatus usually are composed of a bed that represents the formation fracture; where fluid mixed with LCMs flows through this bed under a specific pressure and the LCMs try to form a seal to prevent fluid loss. The beds can be slot or tapered discs, as seen in Figure 2.2b-2.2e, which represent either natural or induced fractures. They can also be ceramic discs that provide porous formations (Al-Saba *et al*, 2014).

Al-Saba *et al*. (2014) and Mostavafi *et al*. (2011) tested the LCM sealing efficiency using HPHT-PPA. The LCM sealing efficiency in this experiment was based on the total fluid loss and the maximum pressure the seal can withstand before breaking. They tested different size distributions, fracture sizes and LCM concentrations. Both of the experiments were able to handle up to 10,000 psi and 300 degrees Fahrenheit. Having such an apparatus is effective for imitating conditions in the bottomhole. Matsui *et al*. (2012) also tested LCMs using the HPHT-

PPA and analyzed the results based on seeing the highest temperature and pressure at which the seal can withstand before breaking.

According to White (1956), gravel, sand and marbles can also be other types of beds that fluid loss can be tested on. The type of bed used depends on the conditions that are expected in the bottomhole and each bed under different pressures provides different results. For example, fibrous materials seal ceramic discs efficiently and therefore are usually used in porous formations. While granular materials are not as good with ceramic discs but can seal slot discs efficiently. Therefore, granular materials should be used for sealing bigger fractures (White, 1956).

Figure 2.1. High Pressure and High Temperature Permeability Plugging Apparatus

Sanders *et al*. (2010) modified the PPA by trying to determine if the LCM can withstand high shear stress. The main objective of the experiment was to see the maximum shear stress that the LCM can hold before the particles decrease in size and the bridges break. This was tested by a method named the Push-out test where a hydraulic piston pressure is applied at a constant rate and the LCMs are monitored. Whenever the LCMs decrease in size, this will be the highest shear stress that they can withstand.

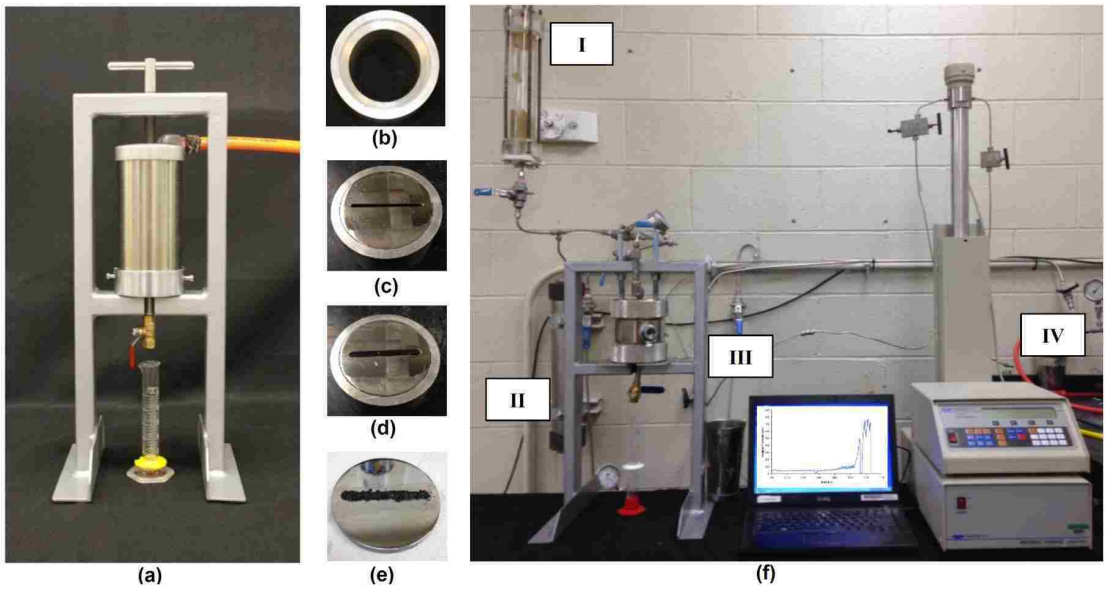

Figure 2.2. (a) Low pressure LCM testing particle plugging apparatus (b) Snug-fit spacer, (c) TS1, (d) TS3, (e) Sealed tapered disc, (f) Modified particle plugging apparatus (I) Plastic accumulator to transfer drilling fluid to ii. II) A metal accumulator used to inject fluids into the cell. III) HPHT Testing Cell that holds pressures up to 10,000 psi. Can also be heated till up to 300 degrees F using the heating blanket. (The PPA modification) IV) ISCO pump (DX100) used for fluid injection and connected to a computer for data logging. (Al-Saba *et al*, 2014)

2.4 Wellbore Strengthening

Wellbore strengthening in the case of lost circulation focuses on increasing the fracture gradient and therefore, allows the mud weight window to be increased. To be able to understand how mud is lost to the formation and how to strengthen and stabilize the wellbore, the stresses around the wellbore need to be analyzed. In an isotropic stress field there are 3 different types of stresses

acting around the wellbore. These are the vertical overburden stress (σ_V) occurring from the layers above the formation, the maximum horizontal stress (σ_H) and the minimum horizontal stress (σ_h). Whenever mud pressure becomes too high, tensile stresses occur at the wellbore and a fracture becomes induced perpendicular to the σ_h direction as seen in Figure 2.3. Whenever such fracture is induced, lost circulation occurs and needs to be treated.

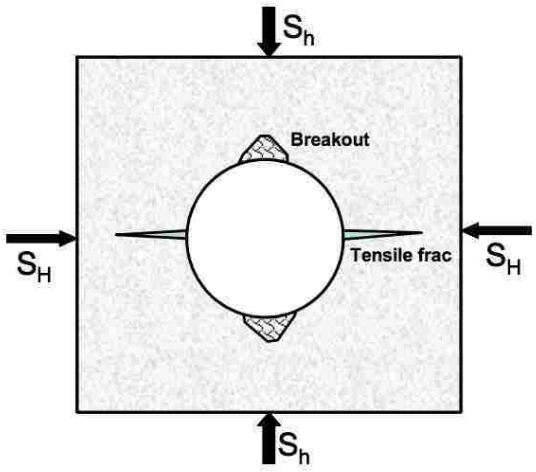

Figure 2.3. Horizontal stresses acting on the wellbore

Considering a vertical well in an anisotropic stress field, the stresses around the wellbore could be defined in the radial (r) and tangential direction (θ) (Peng and Zhang, 2007). They are defined in Equations 2.1 and 2.2 as follow:

$$\sigma_r = \frac{(\sigma_H + \sigma_h)}{2}\left(1 - \frac{R^2}{r^2}\right) + \frac{(\sigma_H - \sigma_h)}{2}\left(1 - \frac{4R^2}{r^2} + \frac{3R^4}{r^4}\right)cos2\theta + p_m\frac{R^2}{r^2} \tag{2.1}$$

$$\sigma_\theta = \frac{(\sigma_H + \sigma_h)}{2}\left(1 - \frac{R^2}{r^2}\right) - \frac{(\sigma_H - \sigma_h)}{2}\left(1 - \frac{4R^2}{r^2} + \frac{3R^4}{r^4}\right)cos2\theta + p_m\frac{R^2}{r^2} \tag{2.2}$$

Where R is the wellbore radius, r is the distance from the wellbore, p_m is the mud weight and θ is the angle at which the stresses are acting. After knowing these stresses, the Terzaghi effective stress theory can be applied and it includes temperature and pore pressure effects (p_p). The effective stresses that are in the tangential direction ($\sigma_{\theta'}$) are also known as the hoop or circumferential stresses around the wellbore. The hoop stresses are the stresses of most interest when trying to prevent or treat mud losses. According to Peng and Zhang (2007), the effective tangential stress for a vertical well in an anisotropic stress field can be defined by Equation 2.3 as:

$$\sigma_{\theta'} = \sigma_H + \sigma_h - p_p - p_m - \sigma_T - 2(\sigma_H - \sigma_h)cos2\theta \tag{2.3}$$

Where σ_T is the thermal stress due to temperature effects and can be defined in Equation 2.4 as:

$$\sigma_t = \frac{\alpha_T E \Delta T}{1 - v} \tag{2.4}$$

It can be seen that the only parameter that the drilling engineer can control in Equation 2.3 is the mud weight (p_m). When the mud weight becomes too high, it can be seen that the tangential stress decreases. Whenever the tangential stress starts to become negative or goes in tension, this is when the fracture is induced. Lost circulation materials are supposed to increase the tangential stress by isolating the fracture from the wellbore. Increasing the tangential stress will prevent the fracture from propagating and prevent fluid losses. The smart LCM as mentioned above has the

ability to seal the tip of the fracture and cause compressive stresses on the wellbore due to its expansive properties. These forces increase the effective tangential stress and therefore lead to wellbore strengthening.

2.5 Understanding and Modeling LCM Performance

2.5.1 Wellbore Hoop Stress Enhancement and Strengthening Theories

Enhancing the stress around the wellbore is a part of our proposed smart LCM. This section will therefore describe the different types of theories that have been proposed to strengthen the wellbore and increase the stress around the wellbore. Wellbore strengthening theories is a set of techniques that could increase the fracture gradient by effectively sealing and plugging fractures using LCMs. (Salehi and Nygaard, 2012).

Fuh *et al*. (1992) tested LCMs performance using theoretical approaches and field trials. They created a fracture pressure inhibitor model. This model suggested that LCMs screen out at the fracture tip, form a seal and increase fracture initiation and propagation pressures. Van Oort *et al*. (2011) introduced the fracture propagation resistance model using results presented by Morita *et al*. (1990). The model also suggests that when the fracture tip is isolated and sealed by the LCM, the fracture propagation pressure increases and therefore, the wellbore is strengthened due to the increase in the mud weight window.

Dupriest (2005) introduced the fracture closure stress model. This model describes the stress on the fracture plane that keeps the fracture faces in contact. Increasing the fracture width and sealing the fracture tip could increase this stress. When the fracture tip is sealed, adjacent rocks are compressed and near wellbore hoop stresses change. Therefore, a lot of theories have focused more on fracture tip sealing. However, Alberty and Mclean (2004) presented a stress cage model using linear elastic fracture mechanics model. The model explains that the hoop stress around the

wellbore is enhanced and increased when LCMs seal the fracture mouth. Salehi (2012) tested the wellbore hoop stress enhancement theory using a 3D poro-elastic, finite element model. This model simulated initiation, and propagation pressures of the fracture when the mouth is sealed. Simulation results showed that if the fracture mouth is effectively sealed, the hoop stress around the wellbore would be increased and restored. Therefore, researchers have come up with theories to see which out of the fracture mouth or tip if sealed will be the most effective.

Aadnoy and Belayneh (2004) presented the elastic-plastic fracture model. This model explains how fracture propagation can be decreased through plastic deformation of the mud cake building a seal on the fracture's mouth. The material type and number of particles used affected the fracture propagation pressure significantly. Using this model, the right concentration to seal the fracture efficiently can be picked accordingly.

2.5.2 Bridging of Particles in Flow

Bridging of particles is defined as buildup of solids in porous formations. Bridging mostly occurs from cohesion between particles and this happens because of electrostatic forces, capillary forces or Van Der Waal forces (Israelachvelli, 2015).

Electrostatic forces occur when there is friction between particles. This friction causes electrons to be transferred from one particle to another, which therefore leaves the particles with some sort of charge. These forces can still occur even if there is no contact between particles and the distance between these particles is relatively long. (Rhodes, 2008). Coulomb's Law describes the most dominant electrostatic force that causes particles to be charged and this dominant force could be referred to as the Coulomb force. Seville *et al.* (2012) describes the Coulomb force to be

$$F_{ES} = \frac{Q_1 Q_2}{4\pi S^2 \epsilon_r \epsilon_o} \tag{2.5}$$

Where Q is the particle charge, S is the distance between the centers of the particles, ϵ_r is the free space permittivity and ϵ_o is the interstitial fluid's relative permeability. Capillary forces occur due to the formation of liquid bridges between particles. (Rhodes, 2008). The capillary forces are given by

$$F_{Capillary} = 2\pi\beta\gamma R sin^2[1 + \frac{R\Delta P}{2\gamma}] \tag{2.6}$$

Where β is half of the filling angle, γ is the fluid's surface tension, R is the radius of the particle and P is the pressure. Since the particles will be moving with a special velocity when submerged in the fluid, viscous forces need to be accounted for. Viscous forces can be split into a tangential force and a normal force. The tangential force is described by Goldman *et al.* (1967) to be

$$F_{Vtangential} = 6\pi R v_t \mu(0.9588 + \frac{8}{15} ln \frac{R}{S}) \tag{2.7}$$

Where v_t is the tangential velocity of the particles, μ is the viscosity of the liquid between the particles and S is the distance between the particles. The normal viscous force is described by Adams and Perchard (1985) to be

$$F_{Vnormal} = 6\pi R v_n \mu \frac{R}{S} \tag{2.8}$$

Where v_n is the normal velocity of the particles. Finally, Van Der Waal forces occur when electrostatic attractions are induced between the molecules in the particles. These forces depend on the molecules' spacing within the particles. They occur due to the rearrangement of electrons in their orbitals which leads to the molecule to have opposite charges on each side

(Israelachvelli, 2015). According to Seville *et al.* (2012) the Van Der Waal forces occurring between the particles are given by

$$F_{VDW} = \frac{dW(S)}{dS} \tag{2.9}$$

Where W is the potential for two molecules to pair up. Seville *et al.* (2012) suggests that given an entire body and integrating the interaction of the molecules will derive Van Der Waal forces that can work for larger distances. Therefore, calculating the Van Der Waal forces between the particles and the surface of the body is done by

$$F_{VDW} = \frac{RA}{12S^2} \tag{2.10}$$

Where R is the particle's radius, S is the distance between the surface of the body and the particle and A is a Hamakar constant that describes the particles' interactions and relies on the density of the particles.

2.5.3 Particle Size Selection Theories for Bridging

Picking the correct LCM size can increase the chance for the LCMs to bridge and seal the fracture. Various bridging theories for LCMs are available and their main goal is to increase the particles' capability to bridge and seal the fracture.

Abrams (1977) proposed a theory to minimize formation damage due to lost circulation and mud invasion. Knowing the average size of the formation's pore throat, the LCMs average size should be equal to or larger than a third of the pore size. The concentration of LCMs in the mud formulation should be larger than 5% of the volume of the total solids added to the mud.

Whitfill (2008) proposed another theory to optimize LCM selection and ensure bridging and sealing of the fracture. The LCM's average size should have the same size as the fracture width to make sure that the fracture is effectively plugged.

Vickers (2006) suggested that D10, D25, D50, D75 and D90 should all be taken into consideration when picking the diameter of the LCM particle. He suggests that 1) 90% of the LCMs added to the mud should be greater than the smallest pore size 2) 75% of the LCMs added should have a size that is a seventh of the average pore size 3) 50% of the LCMs added should have the sizes that were suggested by Abrams (1997) 4) 25% of the LCMs added should have sizes that are less than two third of the largest pore size 5) 10% of the LCMs added should have sizes equal to the largest pore size.

2.5.4 Fracture Width and Length Modeling

Fracture width estimation and modeling is very important when it comes to picking the right size of LCM. A lot of research and models have been made to try and estimate the fracture width.

Alberty and McLean (2004) created a 2-D line fracture solution, shown in Equation 2.11, which compares fracture width results to finite element analysis results. They created this solution through applying theories from continuum fracture mechanics. The solution could estimate the fracture width at any distance form the mouth of the fracture. However, the length of the fracture needs to be known in order to estimate the fracture width

$$W = \frac{4(1-v^2)}{E}(p_w - \sigma_H)\sqrt{(L + r_w)^2 - x^2}\,, \tag{2.11}$$

Where W is the fracture width, v is the Poisson Ratio, E is the Young Modulus, p_w is the wellbore pressure, σ_H is the maximum horizontal stress, L is the length of the fracture, r_w is the wellbore radius and x is any distance from the fracture mouth.

Wang *et al*. (2008) developed a semi analytical solution for fracture width and length as seen in Equation 2.12. They modified an earlier work done by (Deeg and Wang, 2004). In this equation p_0 stands for pore pressure. The length (L) and width (W) in the equation can be calculated by having a system of two equations and two unknowns from which in the first equation the stress intensity factor of the fracture is known and the second equation the critical intensity factor of the formation is known.

$$W = \frac{8(1-\nu^2)L}{\pi E}\left[\frac{\frac{\pi}{2}a(p_0-\sigma_H)+(p_w-p_0)(ab+\sum_{n=1}^{\bowtie}\sin(2nb)(2\,\mathrm{acos}(2nb)+\frac{r_w\sin(2nb)}{Ln}}{(2n-1)(2n+1)}\right] \quad (2.12)$$

Where a=$\sqrt{1-(\frac{r_w}{L})^2}$, and b= $sin^{-1}(\frac{r_w}{L})$. Using both equations 2.11 and 2.12, an estimated fracture width under specific bottomhole conditions can be picked to simulate particle bridging and plugging of LCMs.

2.6 Shape Memory Polymers

The shape memory effect was first discovered by Chang and Read in 1932. Shape memory polymers (SMPs) are polymers that have the ability to be deformed and fixed into a temporary shape. They are then able to recover to their original permanent shape only when they are exposed to a specific external stimulus such as light, magnetic field, temperature, moisture, or pH. Not all polymers can be fixed in a temporary shape. For example, rubber can change shape whenever it's loaded, but when the load is removed the rubber goes back instantaneously to its original shape and no fixing of the temporary loaded shape has occurred. However, when the shape memory polymers are deformed when loaded, they have the ability to trap mechanical energy as internal energy, and release this energy whenever an external stimulus causes a change in the molecular relaxation rate or in material morphology (Li, 2014). Shape memory polymers

do not only have this shape-changing advantage but they are also cheap, lightweight, nontoxic, biocompatible and biodegradable (Ratna and Karger-Kocsis, 2008).

The smart LCMs proposed in this thesis will have temperature as an external stimulus. Shape memory polymers with temperature as an external stimulus can be either thermoset or thermoplastic. Thermoset SMPs are physically or chemically cross-linked polymers. They are usually preferred in engineering structures due to their high stiffness, high strength, high thermostability, high dimensional stability and high corrosion resistance as compared to thermoplastic SMPs. During the shape recovery process, thermoplastic SMPs melt when exposed to very high temperatures and therefore, may not be a good chemical to use for the smart LCM. The smart LCMs proposed here will have characteristics that stand between the thermoset and thermoplastic SMPs and is called an anionic SMP.

Before explaining how the smart LCM will recover, seal fractures and strengthen the wellbore, there is a process called SMP programming that needs to be done to achieve such advantages. Programming is the process that fixes the SMP in the temporary shape. A five-step thermomechanical cycle can explain how the SMP is programmed as seen in Figure 2.4.

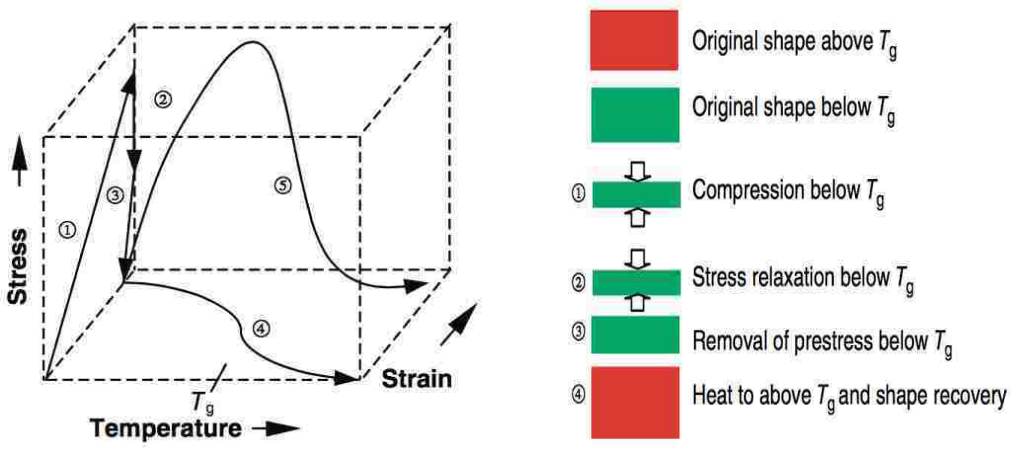

Figure 2.4. Cold-Programming for thermoset SMPs (G. Li, 2014)

Such programming is called cold programming because the programming is conducted in the glassy state (Li and Xu, 2011; Li *et al*., 2013). From Figure 2.4, the original shape of the SMP is pre-stressed and put under compression at a temperature below the glass transition temperature (T_g). The glass transition temperature is the temperature at which the SMPs go from being in a glassy state to a rubbery state. The second step is called stress relaxation and it happens while keeping the strain constant but relaxing the stress. The third step is removing the load. This completes the programming. As for recovery, it has two representative modes. One is free shape recovery, as shown in the fourth step in Figure 2.4. This happens whenever the SMP is heated to above T_g. It can also show stress recovery, as illustrated in step 5 in Figure 2.4. Step five happens when the recovery is constrained and it is called constrained overall stress recovery.

Noticing the programming of the shape memory polymers, it can be seen that such shape-changing properties will benefit the smart LCM to seal big fractures without plugging drilling tools or damaging production zones. The smart LCM will be small in size when entering the tool and then expand at a specific temperature within the fracture due to the difference between mud and formation temperature. Therefore, sealing the fracture and preventing plugging of tools. Because the smart LCM will also have stress recovery due to the constraint expansion, these compressional forces can strengthen the wellbore.

Siskind and Smith (2008) developed an equation to calculate the overall stress recovery from the SMP. Equation 2.13 shows the overall stress recovery from the SMP. The authors explain that the SMP has an initial volume and when this volume changes due to temperature there will be a frozen volume portion ($\emptyset_f$) and an active volume portion ($\emptyset_a$). The active volume is the sum of the strain from the entropic and thermal components, while the frozen volume is the stable shape recovery. The active volume represents the portion of rubbery state of the SMP

while the frozen volume represents the glassy state of the SMP during shape transition at a specific temperature. The strains from both components are then subtracted from the total strain (ϵ) of the SMP and multiplied by the Young's Modulus (E) to calculate the overall stress recovery of the SMP. The total strain can be calculated using Equation 2.14.

$$\sigma_{overall} = E(\epsilon - \int_0^{\emptyset_f} \epsilon_f^e(x)\, d\emptyset - \int_{T_0}^{T_g} [\emptyset_f \alpha_f + (1-\emptyset_f)\alpha_a] dT) \tag{2.13}$$

$$\epsilon = \frac{1}{V}\int_0^{V_{frz}} \epsilon_f^e\, dV + [\emptyset_f \epsilon_f^i + (1-\emptyset_f)\epsilon_a^e] + [\emptyset_f \epsilon_f^T + (1-\emptyset_f)\epsilon_a^T] \tag{2.14}$$

Where ϵ_f^e is the entropic frozen strain, x is a position vector, T_0 is the initial temperature, α_f is the thermal expansion coefficient for the frozen portion, α_a is the thermal expansion coefficient for the active portion, T is the temperature, $\emptyset_f$ is the frozen fraction, V_{frz} the actual frozen volume, V is the total volume, ϵ_f^i is the internal energetic strain in the frozen portion, ϵ_a^e is the stress induced entropic strain in the active portion, ϵ_f^T is the thermal strain in the frozen portion and ϵ_a^T is the thermal strain in the active portion.

Liu *et al.* (2006) developed another equation to calculate the overall stress recovery of the SMP, which is given as

$$\sigma_{Overall} = E\,(\,\varepsilon - \varepsilon_s - \int_{T_h}^{T} \alpha dT\,) \tag{2.15}$$

Where ε is the total strain, ε_s is the strain from the free strain recovery test, T_h is the maximum temperature, T is the temperature, α is the thermal coefficient and E is given by Equation 2.16 as

$$E = {}^{1}\Big/\left(\frac{\emptyset_f}{E_i} + \frac{1-\emptyset_f}{E_e}\right) \tag{2.16}$$

Where E_i is the Young' modulus related to the internal energetic deformation, E_e is the Young's modulus related to the entropic deformation and $\emptyset_f$ is the volume fraction of the frozen phase given by Equation 2.17 as

$$\emptyset_f = \frac{\varepsilon_s}{\varepsilon_{pre}} \tag{2.17}$$

Where ε_{pre} is the pre-strain. According to Wang and Li (2015), the overall stress recovery can be divided into four components: relaxed stress, thermal stress, memorized stress and residual programming stress. The relaxed stress occurs due to the particles being constrained from expansion and it reduces the overall stress recovery. The relaxed stress is given in Equation 2.18 to be

$$\sigma_{Relaxed} = \sigma_{eff}(1 - \sum_{i=1}^{n} \exp(-\frac{t}{\tau_i})) \tag{2.18}$$

Where σ_{eff} is the effective relaxed stress, t is the time and τ_i is the effective relaxation time. The thermal stress occurs due to temperature rising. Since this is a constrained environment and free expansion is prohibited, thermal stress is released. Thermal stress can increase or decrease the overall stress based on the type of programming occurring. For example, it can be seen in Figure 2.4 that the stress in step 5 will peak then decrease again; this peak is because of the thermal and entropic stresses. Subtracting the thermal stress will give a constant and more reliable stress release from the SMP. The thermal stress is calculated in Equation 2.19 to be

$$\sigma_{Thermal} = \int_{T_0}^{T_r} E(T)\alpha(T)dt \tag{2.19}$$

Where α is the thermal coefficient, T is the temperature and E(t) is given by Equation 2.16. The memorized stress is the stress produced in the loading phase of the shape memory polymer. It is calculated by

$$\sigma_{memorized} = E(T).\varepsilon_r.(1 - \emptyset_f) \tag{2.20}$$

Where ε_r is the strain that occurs when the particle undergoes free recovery. Finally, the residual programming stress is considered to be zero whenever there is an unloading phase in the programming of the SMP. The overall recovery stress in a confined environment is given by

$$\sigma_{overall} = \sigma_{Thermal} + \sigma_{memorized} + \sigma_{residual} - \sigma_{relaxed} \tag{2.21}$$

Li and Xu (2011) tried to calculate the memorized stress by considering the stress relaxation effect during stress recovery. They proposed that the memorized stress is the difference between the measured stress by the MTS machine and the thermal stress and stress relaxation. They used a simple stress relaxation equation to calculate the relaxed stress.

According to Li (2014), the relaxed stress was measured using an MTS Q-TEST 150 machine with a fully constrained recovery. Figure 2.5 shows the relaxed stress of the SMP in particle form versus foam (Li and Nettles, 2010).

Both of these SMPs were also pre-stressed with two different stress values. It can be seen that the more the SMP is pre-stressed, the higher the relaxed stress. The relaxed stress is unstable and should therefore be subtracted for a more stable overall stress recovery. Even after all of these subtractions are made the SMP can release up to 13 MPa of stress in porous media, meaning that it will cause compressional forces on the wellbore hoop stress. These compressional forces could help prevent the hoop stress from going into tension and could lead to wellbore strengthening. Finally, whenever a bundle of SMPs are present and are activated above T_g, their rubbery state

allows them to bridge and connect together, forming an effective strong seal that isolates the fracture from the wellbore. When activated, the shape memory polymers use their ductility property to form bridges that are extremely hard to break (Li, 2014). Therefore, there is a stress recovery advantage and a bridging advantage for having LCMs made out of SMPs.

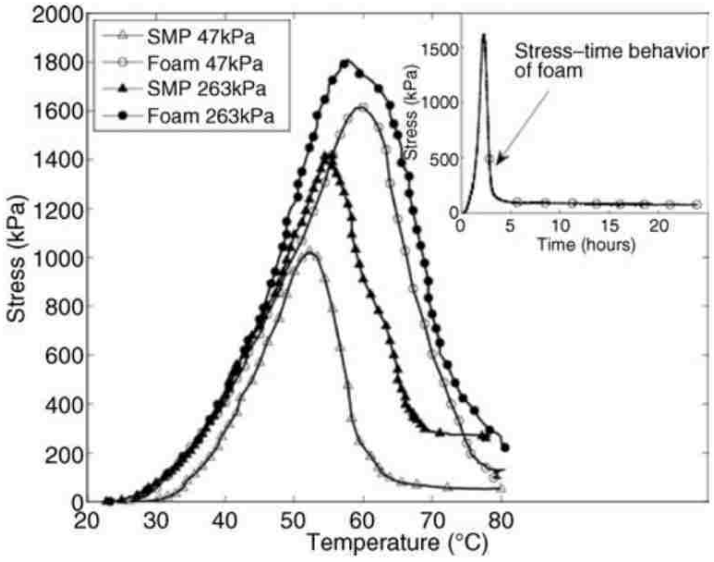

Figure 2.5. Measured stress of different types of SMPs pre-stressed at different values (Li and Nettles, 2010).

It is also important to note that the smart LCMs will float in the mud due to their density. Adding surfactants to reduce the surface tension of the mud and disperse the particles will prevent such floating from occurring. SMPs have also been used as proppants (Santos *et al.*, 2016), for re-fracturing operations (Santos *et al*., 2017) and in cementing applications (Taleghani *et al*., 2017).

Chapter 3: Experimental Procedure

The objective of running this experiment is to create a field environment of lost circulation at a small scale and see how effective our smart expandable LCM will seal it. This chapter describes the apparatus used to evaluate lost circulation, the LCM used and the procedures made. The apparatus components can also be seen in Appendix B.

3.1 Experimental Design

The experiment done to test the smart LCMs was permeability plugging apparatus (PPA) as seen in Figure 3.1.

Figure 3.1. HPHT PPA with LCM Receiver

The permeability plugging apparatus that was used is a high-pressure high-temperature instrument that has a maximum operating temperature of 500 degrees Fahrenheit and a maximum operating pressure of 5000 psi. The PPA assembly consists of a hydraulic hand pump assembly to supply pressure, a 5000 psi stainless steel PPA cell where the fluid and LCM will be placed as seen in Figure 3.2, a PPA heating jacket to heat up the apparatus to specific temperatures, a dial thermometer to measure the temperature, a LCM PPA Receiver to measure fluid loss through its collection valve as seen in Figure 3.3, a backpressure receiver and this is

used only if the temperature exceeds bubble point of the fluid, a carbon dioxide pressurizing assembly or nitrogen pressurizing assembly to work with the backpressure receiver, a graduated cylinder to measure the fluid loss and finally, slot discs and tapered discs to represent fractures.

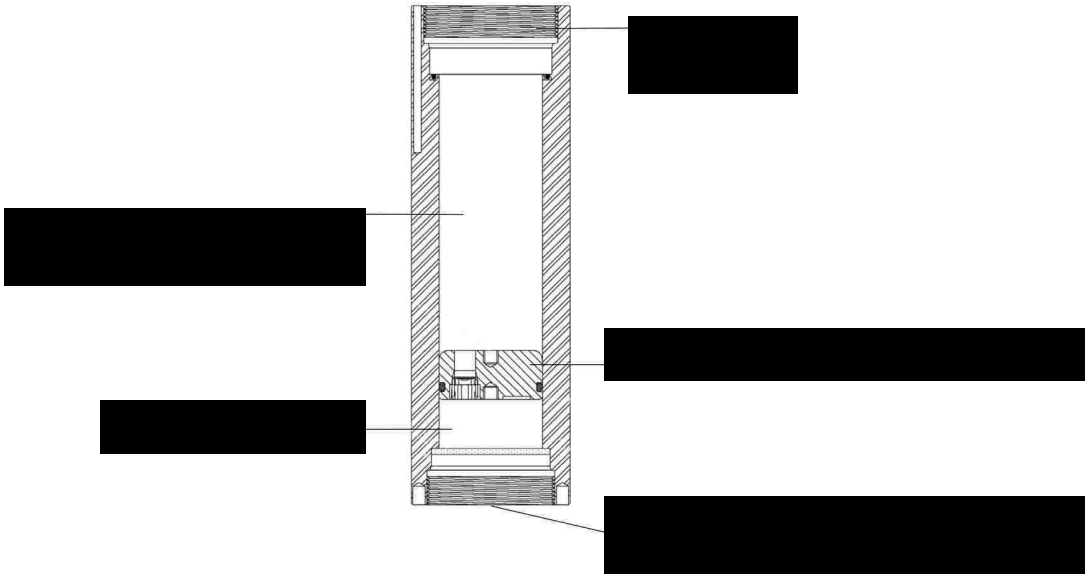

Figure 3.2. PPA cell schematic

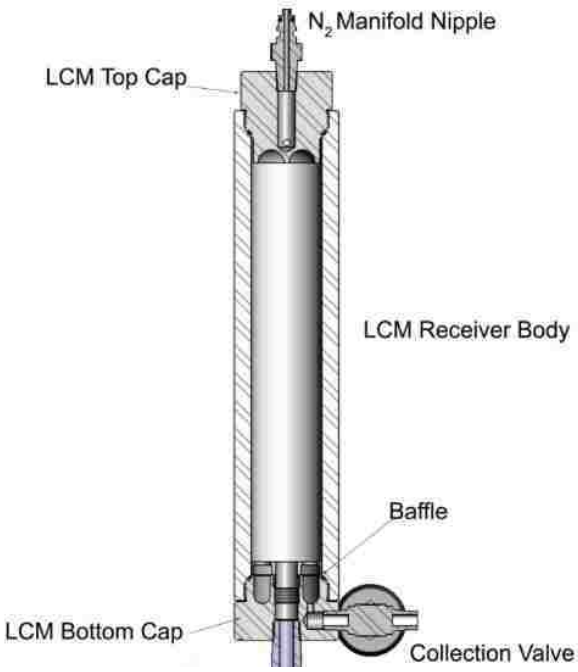

Figure 3.3. PPA LCM receiver schematic

3.2 Smart LCMs

The lost circulation material used in these experiments is made out of anionic shape memory polymers. The smart LCMs have a disc shape and their activation temperature is 70℃. This is the temperature where the smart LCM starts to expand. Figure 3.4 shows the smart LCMs before and after activation.

Figure 3.4. (a) Smart LCM before activation (b) after activation.

The smart LCMs have a density of 950 kg/m^3, Poisson's Ratio of 0.4, pre-strain (the maximum strain the LCM can achieve) of 25% and Young's Modulus of 655 MPa, 260 MPa, 2.4 MPa at temperatures of -23℃, 23℃ and 80℃ respectively. All experiments were done with the same type of smart LCMs.

3.3 Experimental Procedure

The drilling fluid was made by adding 38 grams of bentonite to 350 ml of water. The mud had a density of 8.9 ppg and its formulation can be seen in Table 3.1.

Table 3.1. Mud formulation

Products	lb/gal	% By weight	%By volume
Water	8.35	90.19	95.76
Bentonite	21.0	9.81	4.25

A mud rheogram was made by an Anton Paar modular compact rheometer to see the behavior of mud with shear stress. The test was made at 23℃ and 80℃. Figure 3.5 shows the shear stress versus shear rate and Figure 3.6 shows the viscosity versus shear rate and the apparent viscosity can be found.

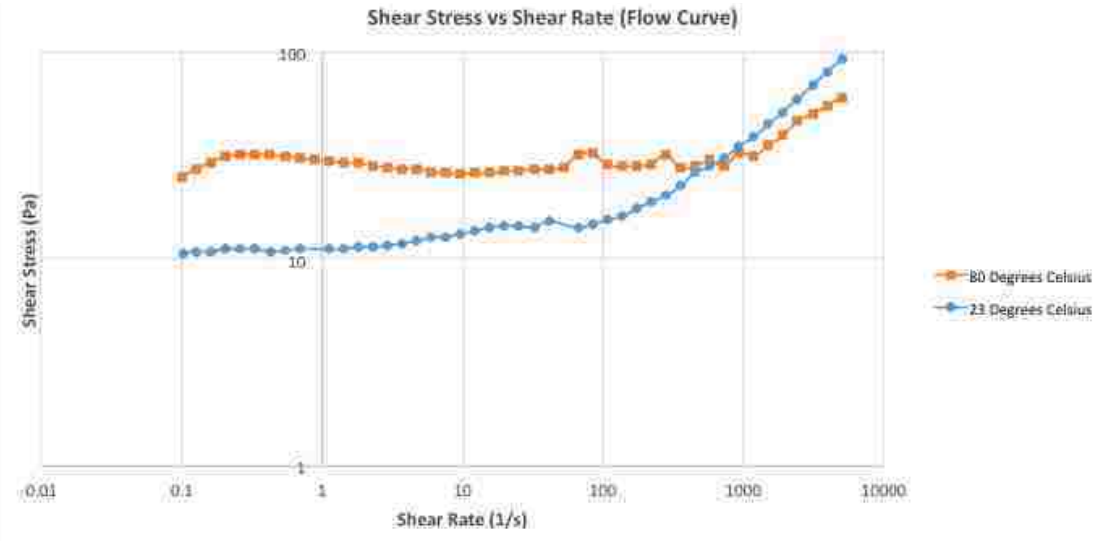

Figure 2.5. Shear stress versus shear rate for the mud used in the experiments

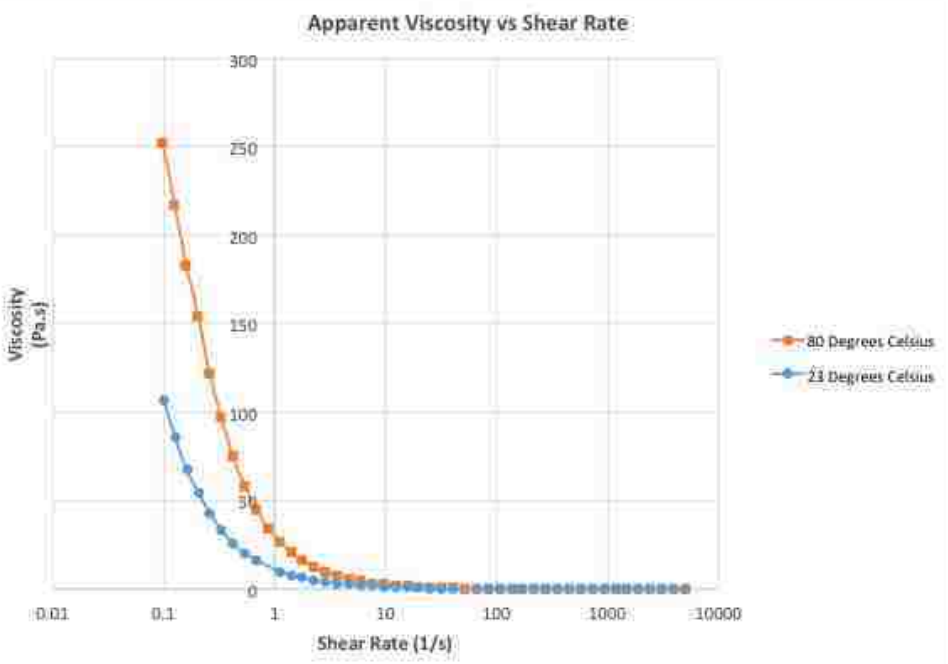

Figure 3.6. Viscosity versus shear rate

170 ml of this mud was taken and the smart LCMs were added to the mud at a concentration of 0.3 pounds of LCM per gallon of mud. This concentration of LCM is equivalent to almost 50 particles. The PPA cell is then filled with this mixture of drilling fluid and LCMs. The particle sizes were varied according to each experiment.

A slot disc or tapered disc as seen in Figure 3.7 is inserted on top of this mixture and on the top of the cell. The slot and tapered disc descriptions can be seen in Table 3.2.

Table 3.2. Dimensions for discs

Type	Length (Inches)	Width (Inches)
Slot Disc	0.279	0.1
Tapered Disc	1.700	0.04 to 0.1

Figure 3.7. a) Slot disc b) Tapered disc

The PPA cell has a floating piston as seen in Figure 3.2 that separates the oil coming from the hydraulic pump from the mixture of mud and LCM. The LCM-Receiver is then tightly capped at the top of the PPA cell. The PPA cell is then inserted in the heating jacket were the temperature is adjusted according to the test made. The hydraulic pump is then connected to the bottom of the PPA cell, where oil pushes the floating piston and if the slot or tapered discs are sufficiently sealed, pressure builds up; if not, then fluid is lost and collected from the collection valve of the LCM-Receiver. Five different tests were made using the PPA and will be discussed in Chapter 5.

Chapter 4: Numerical Simulation

This chapter explains the interaction between fluid, between particles and between a mixture of fluid and particles. This chapter also explains the boundary conditions and the procedures of the numerical model made to test the sealing efficiency of the smart LCMs. It also explains the calculation of concentration of LCMs required to seal a specific size of fracture and the measurement of the compressional forces that will be acting on the wellbore from the LCMs' stress recovery.

4.1 Introduction

Fluid-particle interaction is important when trying to understand engineering applications in granular and porous media. Discrete element method (DEM) and computational fluid dynamics (CFD) have played an important role in understanding the fluid-particle interactions. CFD-DEM method usually solves Darcy's law or Navier-Stokes equation for the CFD part and Newton's equations for particle motion using the DEM part. It also considers force interactions between the CFD and the DEM. An example of these forces will be buoyancy, hydrostatic and drag forces (Zhu *et al.*, 2007).

4.2 Discrete Element Methods

Discrete Element methods is a numerical method that explains granular particle interactions. Cundall and Strack (1979) were one of the first people to propose such a model to help them understand particle interactions and solve tough rock mechanic problems. This simulation generates new contact points as it progresses to be able to adjust for the interaction between particles. The time integration has a smaller time scale than the typical contact time to prevent propagation of the particle disturbance and stop it from going further than its immediate neighbors. The motion of each element is described using Newton's second law.

According to Santos (2016) there are four steps required to finish a DEM simulation. First step includes defining the particles' initial configuration, building the geometry of the shape used and setting its boundary conditions. Second step is where the forces are applied and these forces include gravity, friction between particles and pressures. Third step is calculating the forces that occur due to boundary conditions. This is when the forces mentioned in the previous step lead to the calculation of the velocities and acceleration of particles through solving the momentum equation. Fourth step includes the integration of these forces. The position and velocity of each particle are calculated and updated according to a time step defined by the user. Fifth step is analyzing the results and including thermal and mechanical parameters based on each time step. Each step from 1 to 4 is then repeated until the solution is solved and is complete. Finally, the last step is post-processing and this is the part where the output data is processed to be graphically visualized.

LIGGGHTS is a software used to run the simulation in this paper and it is an improved discrete element code for general granular and granular heat transfer simulations. By solving dynamics equation for particles, LIGGGHTS determines particle interactions, positions and velocities through discrete element method in each time step. LIGGGHTS has an input file that consists of C++ codes with no graphical user interface. When the code is executed, LIGGGHTS creates an output file for each time step. This file contains the particle interactions, velocities and position for each particle at each individual time step. The files are then post-processed so that they can be graphically seen and that the data can be visually interpreted (Santos, 2016).

4.2.1 Governing Equations

In LIGGGHTS, The rotational and translational motions are calculated using equation 4.1. This equation explains how the motion of particle "i" is affected by a wall or by particle "j". The

Hertizian or Hook contact law working with Coulomb's friction law describes the contact behavior of the particles in a DEM simulation (Zhao and Shan, 2013).

$$m_i \frac{dU_i^P}{dt} = \sum_{j=1}^{n_i^c} F_{ij}^c + F_i^f + F_i^g$$

$$I_i \frac{dw_i}{dt} = \sum_{j=1}^{n_i^c} M_{ij} \tag{4.1}$$

Where m_i is the mass of the particle, $\frac{dU_i^P}{dt}$ is the velocity of the particle with respect to time, F_{ij}^c is the particle-particle contact force, F_i^f is the tangential particle-fluid contact force and F_i^g is the gravitational force, I_i is the moment of inertia, $\frac{dw_i}{dt}$ is the change of angular velocity with respect to time and M_{ij} is the torque force.

4.2.2 Heat Transfer Between Particles

Tstory *et al*. (2013) describes the heat transfer in a DEM simulation using the lumped heat capacity approach in a DEM simulation. They state that the heat transfer occurs through conduction between the contact surfaces of the particles and also occurs through conduction between the walls and the particles. The model assumed that the particle temperature is uniform at each time step. Equation 4.2 shows the particle energy equation.

$$m_p c_p \frac{dT_p}{dt} \tag{4.2}$$

Where c_p is the particle thermal capacity, T_p is the particle temperature and m_p is the mass of the particle.

4.3 Computational Fluid Dynamics

OpenFOAM (Open Source Field Operation and Manipulation) is another software used to run the simulations in this thesis and it is a computational fluid dynamics (CFD) simulator. Computational fluid dynamics studies fluid flow through simulations. There are three steps needed to successfully complete a CFD simulation. According to Santos (2016) the first step is setting fluid properties and boundary conditions such as fluid density, fluid viscosity, and pressure at the walls for the fluid to enter. Second the simulation uses finite element method to generate partial differential equations. The partial differential equations are transformed to algebraic equations where they are solved using an iterative method. Each value is calculated based on a discrete place according to the mesh geometry. Finally, the data is post-processed and the solution is graphically visualized.

OpenFOAM divides the fluid domain into cells and variables such as pressure, density and fluid velocity. These variables are then averaged for each cell. The CFD code solves the continuity equation along with the locally averaged Navier-Stokes equation as seen in Equation 4.3 to calculate the variables for each cell and understand fluid motion (Zhu *et al.*, 2007).

$$\frac{d(\emptyset\rho U^f)}{dt} + \nabla.(\emptyset\rho U^f U^f) - \emptyset\nabla.(\mu\nabla U^f) = -\nabla p - f^p + \emptyset\rho g \tag{4.3}$$

Where $\emptyset$ is the porosity, ρ is the density, U^f is the average velocity of the fluid cell, μ is the viscosity, p is the pressure, f^p is the average force that the particle exert on the fluid in a cell and g is the gravitational acceleration.

4.4 Computational Fluid Dynamics and Discrete Element Methods (CFD-DEM)

The CFD-DEM coupling can couple solid particle and fluid system simulations together. The particles' motions are modeled using the discrete element method approach and the fluid flow is

modeled using the CFD approach previously described. Both of these approaches are coupled and a system of solid particles and fluids is formed were the conservation of momentum and mass is achieved (Zhu *et al.*, 2007). Figure 4.1 shows a flowchart to describe the steps required to complete a CFD-DEM simulation.

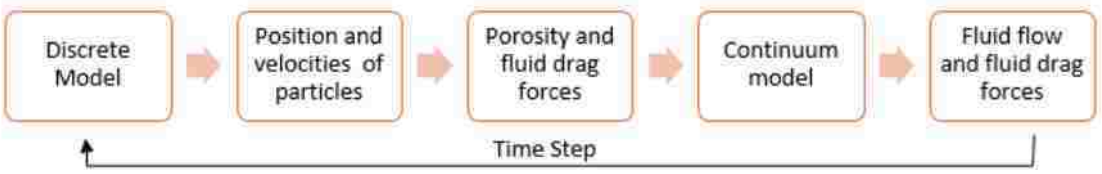

Figure 4.1. Steps to complete CFD-DEM simulation (Santos, 2016)

4.4.1 Particle-Fluid Interaction

Hydrodynamic and hydrostatic forces act on particles whenever they are submerged in a fluid. Hydrodynamic forces include virtual mass force, drag force and lift force. (Zhu *et al.*, 2007). The most dominant out of all forces is the drag force (O'Sullivan, 2011). According to Di Felice (1994), the drag force can be calculated using the following:

$$F_d = C_d \pi \rho_f d_p^2 |V_f - V_p| \frac{V_f - V_p}{8} \varepsilon^{1-x} \tag{4.4}$$

Where,

$$C_d = (0.63 + \frac{4.8}{\sqrt{R_p}})^2 \tag{4.5}$$

$$R_p = \frac{\rho d_p \varepsilon |V_f - V_p|}{\mu} \tag{4.6}$$

$$x = 3.7 - 0.65 \exp\left[\frac{-(1.5 - log R_p)^2}{2}\right] \tag{4.7}$$

Where ε^{1-x} is a function that considers other particles' presence in the system and corrects the equation, C_d is the drag coefficient, ρ_f is the fluid's density, d_p is the particle's diameter size, V_f is the fluid volume, V_p is the particle volume, ρ is the density of the mixture and μ is the viscosity of the mixture.

4.4.2 Particle-Fluid Heat Transfer

Li and Mason (2000) proposed a model to describe convective heat transfer between fluid and particles. This model is described by

$$\frac{\partial T_f}{\partial t} + \nabla.\left(T_f.\mu_f\right) = \nabla.\left(k_{eff}\nabla T_f\right) + S_t \tag{4.8}$$

Where T_f is the fluid temperature, μ_f is the fluid viscosity, k_{eff} is the thermal diffusivity and S_t is a source term and is described by

$$S_t = \frac{q_p}{\rho_f V_{cell}}, \tag{4.9}$$

Where V_{cell} is the volume of the cell, ρ_f is the fluid density and q_p is the heat transfer ratio described by

$$q_p = h\,A_p(T_f - T_p). \tag{4.10}$$

A_p is the area of the particle and h is the heat transfer coefficient calculated through Nusselt number which is a function of Reynolds and Prandtl numbers.

4.5 Simulation Procedure

Four different simulations were made in this paper. The objectives of the simulations as mentioned above were to measure the cumulative fluid loss in a specific sized fracture, the concentration of particles required to seal this fracture and to quantify the compressional stress that will be acting on the wellbore from the stress recovery of the smart LCM.

4.5.1 Simulation Validation

The objective of this simulation is to validate that the results from the simulation are correct and match the experimental results. The steps made to complete this simulation are as follows:

A simulation region in the DEM is defined by building a tapered disc through SOLIDWORKS as seen in Figure 4.2 that has the same dimensions as the tapered disc used in the experiment.

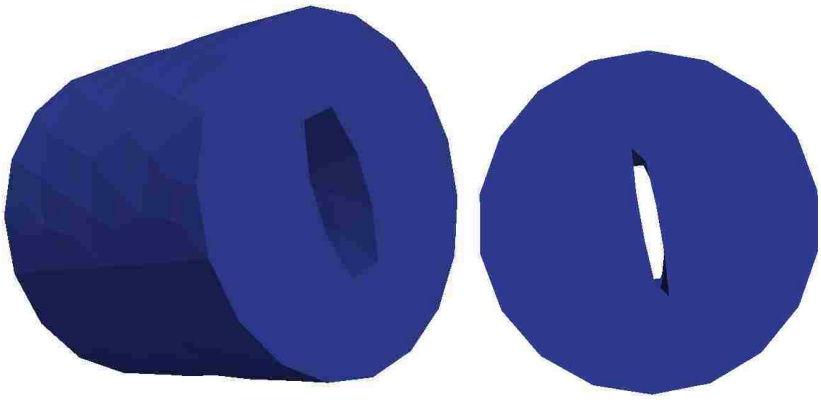

Figure 3.2. Tapered disc designed in the simulation

Pressure at the inlet of the tapered disc was set to 100 psi and pressure at the outlet of the tapered disc was set to zero. The particles were spherical as opposed to discs in experiments and the change in radius leads to change in volume. The particles had properties the same as the ones used in the experiment as seen in Table 4.1. The particles had sizes of 3mm and 5mm at a 1:1 ratio. The particles were mixed with 170 cm^3 drilling fluid that had a viscosity of 15 cp and a density of 8.9 ppg just like in the experiment and they were inserted in the fracture. The viscosity is assumed constant since the shear rate is high.

The initial temperature of the fracture is 72℃ and the temperature increases at a rate of 0.5 ℃/min. when the particles are inserted in the fracture they are activated and undergo thermal expansion. Equation 4.11 gives this thermal expansion.

$$E = \alpha \Delta T \tag{4.11}$$

Where α is the thermal coefficient and ΔT is the change in temperature. The simulation ran for 6.5 minutes and the concentration of LCMs required to seal the fracture, fluid loss versus time and pressure buildup versus time is recorded in the simulation and compared with the experimental results from Chapter 5.1.2

Table 4.1. Properties of the smart LCMs

Properties	Value
Young's Modulus @23℃ (Mpa)	260
Young's Modulus @80℃ (Mpa)	2.4
Poissions Ratio	0.4
Density (kg/m^3)	950
Activation Temperature (℃)	70

4.5.2 Cumulative Fluid Loss

The objective of this simulation is to measure the effectiveness of the seal made by the smart LCMs. The fluid loss is recorded every 30 seconds, if the fracture is sealed then the simulation will stop. If the fracture is not sealed the simulation will keep working and will terminate at 12 minutes. The particles used here had a perfectly spherical shape as opposed to disc shape in the experimental work. Different particle sizes were chosen to form a relationship between particle size and sealing efficiency. Particles with different sizes were also mixed together to see if it is more efficient to use just one size or mix different sizes. Since the fracture will be under pressure in the bottomhole, the amount of its expansion will depend on how much pressure is acting on it. An experiment called strain measurement test that will be discussed in Chapter 5 was made to test the expansion of particles versus pressure. These volumetric expansion values were used in

the simulations to create realistic values of concentrations required. The steps made to complete this simulation are as follows:

A simulation region in the DEM is defined by building a new bigger fracture than the one used in the experiment through SOLIDWORKS. The fracture was in a cuboid box representing the rock and had an elliptical shape with one side having diameters of 40mm and 12mm and the other side has diameters of 20mm and 6mm. The fracture walls are rigid and the length between both sides was 30 cm as seen in Figure 4.3.

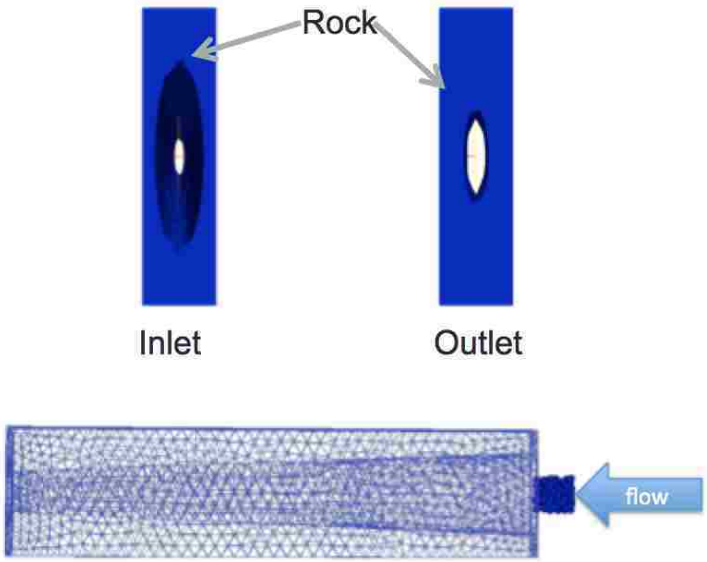

Figure 4.3. Simulation fracture shape where the inlet is on the right side of the fracture and the outlet is on the left side of the fracture

The pressure at the inlet of the fracture and from which the fluid and particles mixture enters was varied. This inlet pressure represents the pressure of the mud and particles at a specific distance beneath the surface. The pressure at the outlet was also varied to keep a constant 200 psi of pressure difference between the inlet and the outlet. The pressure at the outlet is supposed to be the reservoir pressure. The differential pressure represents a realistic amount of pressure overbalance that the well be in when drilled. Table 4.2 shows the pressure variations used in the

simulation. Figure 4.4 shows the inlet pressure of 2000 psi and outlet pressure of 1800 psi for one of the pressure variations.

Table 4.2. Pressure variations in the simulation

	Pressure At The Inlet	Pressure At the Outlet
Case 1	1000	800
Case 2	2000	1800
Case 3	3000	2800

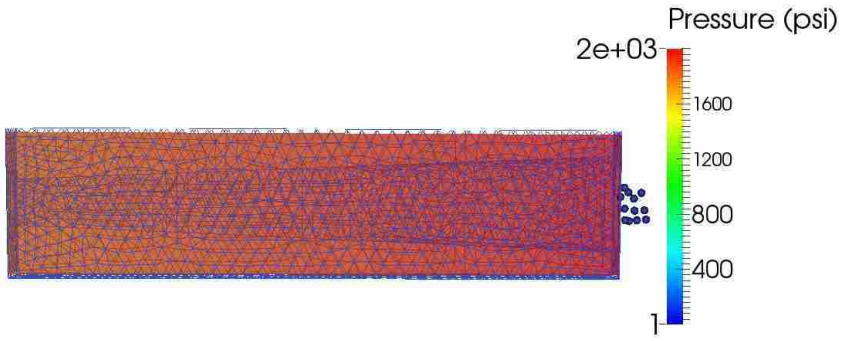

Figure 4.4. Boundary conditions for pressure. Inlet (right side) is set to 2000 psi while outlet (left side) is set to 1800 psi

Four different particle sizes were used in this simulation and they had a diameter of 1.25mm, 1.5mm, 2mm and 2.5mm. A mixture of particle sizes of 1.5mm and 2mm were also used and the mixture had a particle size ratio of 1:1 respectively. The properties of the particles were the same as the properties of the smart LCMs used in the experiment and these properties can be seen in Table 4.1.

The particles were then mixed with 250 cm^3 drilling fluid that had a viscosity of 15 cp and a density of 10 ppg and they were inserted in the fracture. The viscosity is assumed constant since the shear rate is high. The flow rate is calculated in the simulation according to the pressure difference. The initial temperature of the fracture is 70℃ and the temperature increases at a rate

of 5 ℃/min. when the particles are inserted in the fracture they are activated and undergo thermal expansion as seen in Equation 4.11.

The total volumetric expansion allowed for the particle and the thermal coefficient used in the simulation is determined by the experimental strain measurement test in Chapter 5. The temperature stops increasing when the particle has reached its maximum size allowed. The thermal coefficient is considered to be constant because according to Liu *et al.* (2006) the thermal coefficient is a specific constant value below T_g and then increases to a constant value when temperature goes above T_g **.** Figure 4.5 shows the behavior of the thermal coefficient with temperature. Since here the initial temperature of the fracture is 70℃ (T_g) and the maximum temperature is 90℃**,** the thermal strain will remain constant.

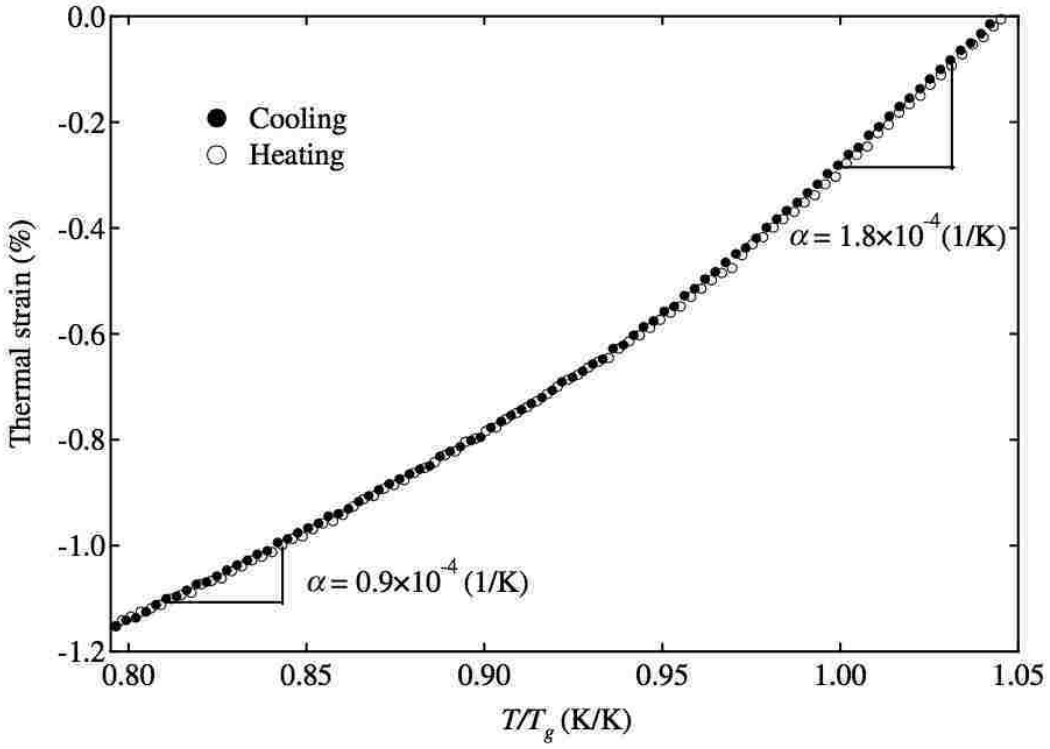

Figure 4.5. Thermal coefficient above T_g

4.5.3 Concentration of Particles Required to Seal The Fracture

For this simulation the objective is to measure concentration of particles in pounds per gallon that are required to seal the fracture. This is achieved by measuring the number of particles that sealed the fracture in Chapter 4.5.2 and converting it into concentration values. Sealing the fracture means that fluid loss is less than 3 cm^3/min.

4.5.4 Stress Recovered from Smart LCMs

The objective of this simulation is to measure the stress recovery of the smart LCM. The same boundary conditions, particle expansion procedure applied in Chapter 4.5.1 are applied in this section too. The particle size used here is only 2mm and the sizes were not varied or mixed. The simulation measured the compressional stress that the particles will cause on the wellbore. This stress was calculated using Equation 2.15.

Chapter 5: Results and Discussions

The objective of this section is to understand how effective the smart LCMs are in sealing the fracture and strengthening the wellbore. This chapter will explain the experimental tests and numerical simulations made and then the results will be analyzed and discussed.

5.1 Experimental Results and Discussions

This section will explain the experimental tests made using the particle plugging apparatus and discuss the results obtained. Five different experimental tests are present in this section.

5.1.1 Sealing Efficiency Test

The objective of this test is to compare fluid loss and pressure buildup below, at and above activation temperature. This experiment is supposed to represent what smart LCMs will do once they get activated in the bottomhole. Therefore, 3 temperatures of 60℃, 70℃ and 80℃ were chosen. The smart LCMs used in this test were a mixture of two different diameter sizes. These sizes were 2.5mm and 5mm from which 0.15 ppg of each smart LCM size was added to 170 ml of water-based mud. The PPA cell was filled with this mixture and the test was done with a slot disc and a tapered disc.

The fluid loss was measured by pumping hydraulic fluid in the cell until pressure started to buildup. The fluid that came out before the pressure buildup is the fluid loss regardless of the time. The maximum pressure buildup is the maximum pressure the seal can hold before the seal is broken and fluid is lost again. Table 5.1 shows the results that were obtained from this experiment.

Table 5.1. Pressure buildup and cumulative fluid loss

Type	Temperature (Degrees Celsius)	Pressure Buildup (Psi)	Cumulative Fluid Loss (ml)
Slot Disc	60	100	47
	70	2000	22
	80	4500	7
Tapered Disc	60	0	58
	70	2500	18
	80	5000	0

It can be seen from the results that below activation temperature (60℃) fluid loss is very high. However, when the smart LCM got activated the fluid loss decreased significantly. At 80℃, all the smart LCMs were activated and the fracture was effectively sealed. The particles bridged together as seen in Figures 5.1 and 5.2 and were able to withstand extremely high pressures.

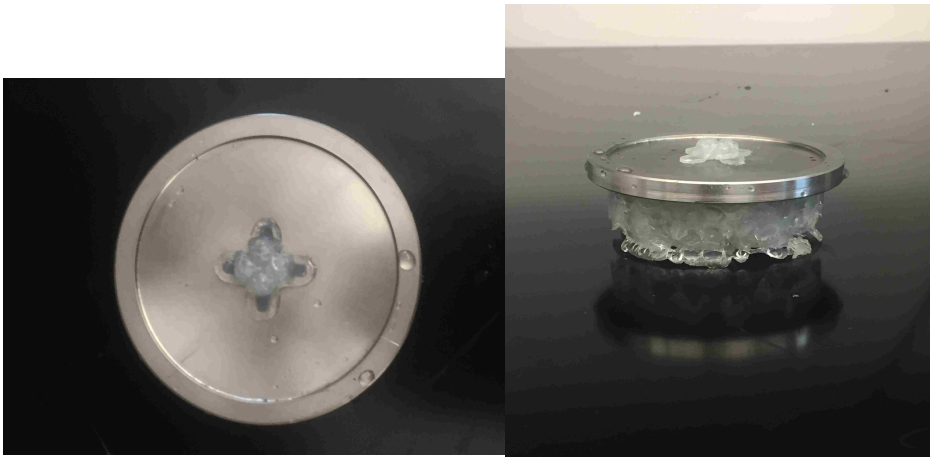

Figure 5.1. Effectively Sealed Slot Disc by the smart LCMs.

Figure 5.2. Effectively Sealed Tapered Disc by the Smart LCMs.

5.1.2 Fluid Loss and Pressure Buildup Test

The objective of this test is to measure fluid loss and pressure buildup once the LCM is activated with respect to time. This experiment is supposed to show the decrease in fluid loss that the drilling engineer will see once the fracture is effectively sealed. The heating jacket was preheated to 75 Degrees Celsius. The smart LCMs used in this test were a mixture of two different diameter sizes. These sizes were 3mm and 5mm from which 0.15 ppg of each smart LCM size was added to 170 ml of water-based mud and inserted in the PPA cell. The PPA cell was then inserted in the heating jacket and left there for 30 minutes before applying pressure, to allow the heat to be transferred to the cell for the activation of the smart LCMs. The fluid loss and the maximum pressure the seal can hold with respect to time were recorded. The fluid loss was measured by pumping hydraulic fluid in the cell at a rate of 1 stroke per 15 seconds. Since the fracture was sealing with time, fluid was being prevented from going through the fracture and the pressure was building up. This pressure build up was also recorded with respect to time. Figure 5.3 shows the results that were obtained from this experiment for the slot disc. Figure 5.4 shows the results obtained from the tapered disc.

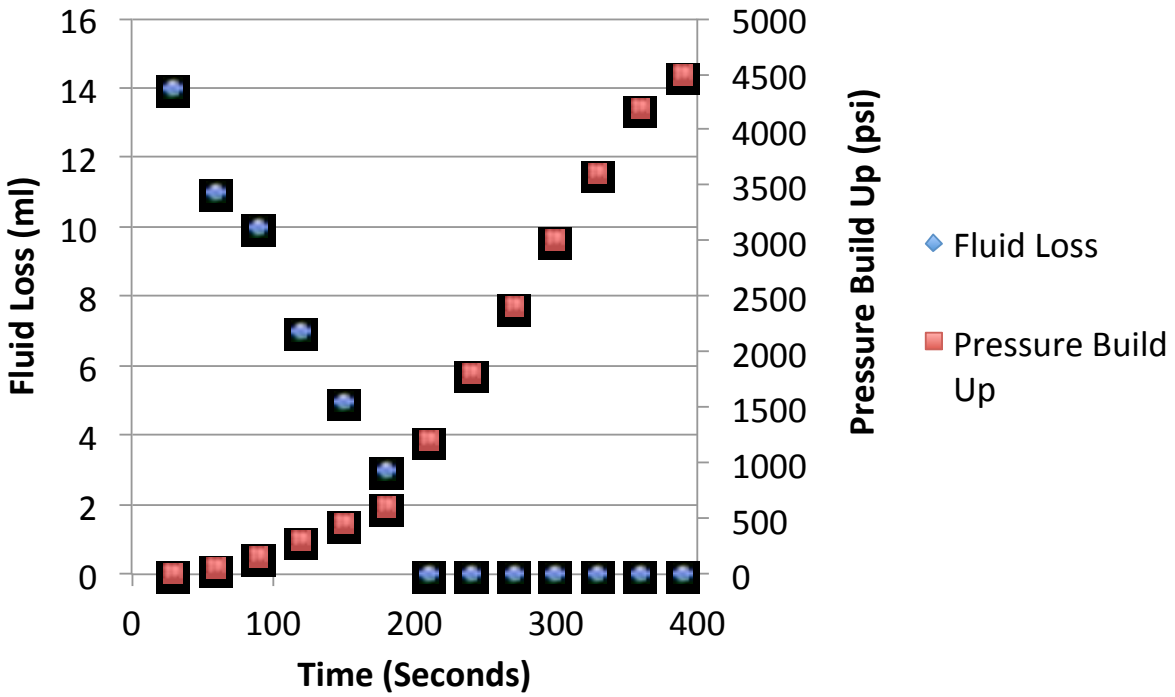

Figure 5.3. Results for slot disc @ 75 Degrees Celsius

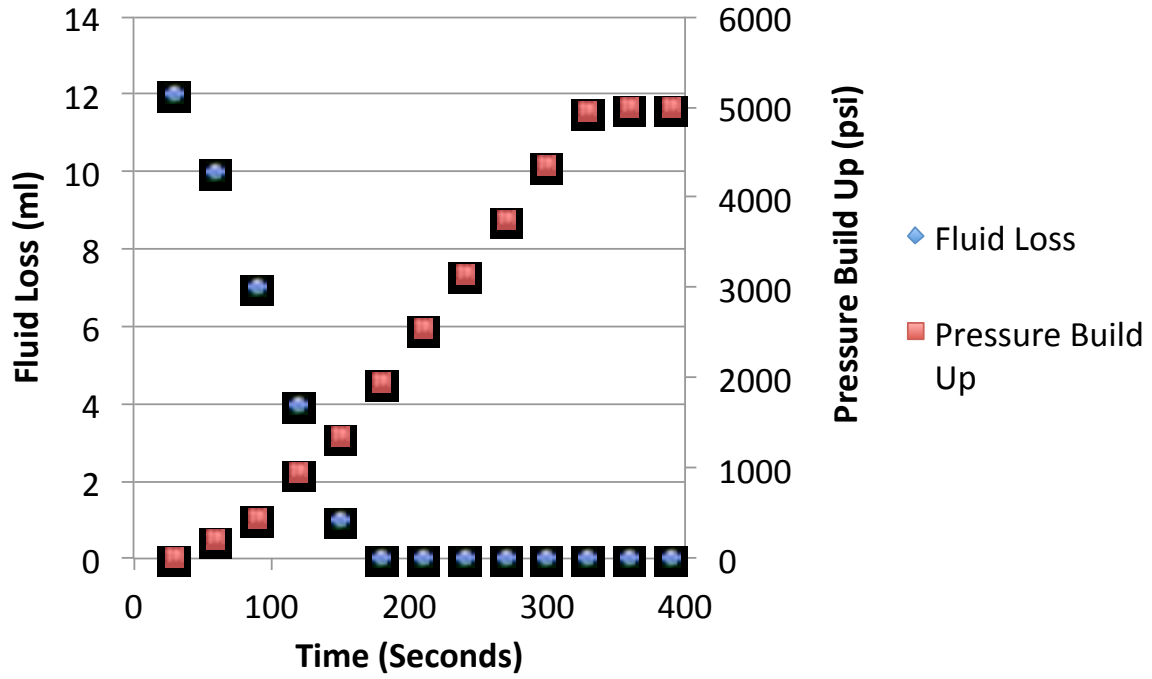

Figure 5.4 Results for tapered disc @ 75 Degrees Celsius

It can be seen from the results that the fluid loss decreased gradually to zero as the particles expanded and started bridging. The seal was very effective and was able to withstand very high pressures.

5.1.3 Strain Expansion Measurement Test

The objective of this test is to analyze the volumetric change property of the LCM as a function of pressure. Since the wellbore is a partially constrained environment, the smart LCM will not be able to fully recover to its shape due to pressure from the bottomhole. Therefore, this experiment will help the drilling engineer understand how the smart LCMs will expand under various pressures. Two particles were picked and their diameter, thickness and mass were measured. These two particles were then mixed with a water-based mud and put in the PPA cell. A disc with no fractures was used instead of a slot disc to allow the pressure to build up in the PPA Cell. Oil was pumped from the hydraulic pump to raise the pressure until 3000 psi and then the temperature was raised to 80℃ and kept constant for 30 minutes. The pressure was then dropped gradually until it reached zero and the particles were then cooled down to room temperature, 23℃. The particles were then taken out from the PPA cell and their diameter, thickness and mass were measured. This experiment was repeated for pressures of 0 psi, 1000 psi and 2000 psi. Each experiment was also repeated twice to decrease the chance of error. It was noticed that there were no changes in mass. Table 5.2 shows the results of the experiments and Figure 5.5 shows the size of the smart LCM before and after expansion at 3000 psi.

The change in volume (dv/v) was calculated by its variation with respect to changes in its radius and thickness as seen in equation 5.1

$$\left(\frac{dv}{v}\right)_{SMP} = 2\frac{\delta r}{r} + \frac{\delta h}{h} \tag{5.1}$$

Table 5.2. Results for the strain measurement test

First Experiment				
	0 psi	1000 psi	2000 psi	3000 psi
Initial Diameter (mm)	5.05	5.21	6.14	4.29
Thickness (mm)	1.82	1.96	2.02	1.81
Diameter After Expansion (mm)	4.82	4.97	5.49	4.2
Thickness After Expansion (mm)	3.36	3.33	2.84	1.95
Dv/v	0.755	0.607	0.194	0.0354
Second Experiment				
	0 psi	1000 psi	2000 psi	3000 psi
Initial Diameter (mm)	5.55	4.91	5.07	5.5
Thickness (mm)	2.39	1.79	2.03	2.01
Diameter After Expansion (mm)	5.23	4.17	4.67	5.47
Thickness After Expansion (mm)	4.65	3.21	2.69	2.07
Dv/v	0.830	0.492	0.167	0.019
Average Dv/v for both Tests				
Average dv/v	0.79	0.55	0.18	0.03

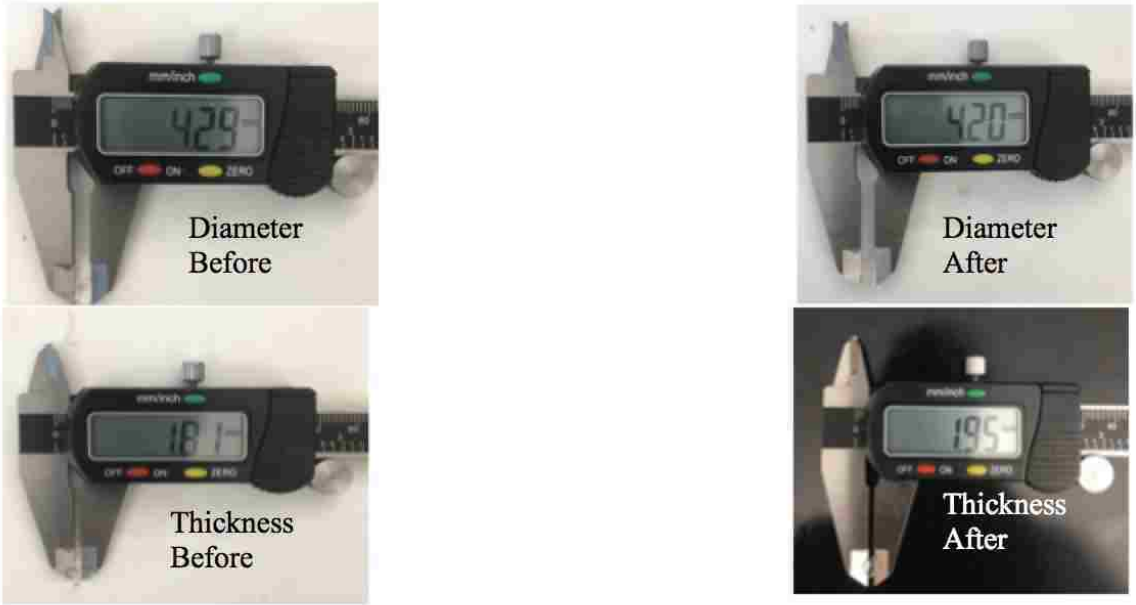

Figure 5.5. Change of Smart LCM size before and after experiment at 3000 psi

The average dv/v was then plotted versus the surrounding hydrostatic fluid pressure as seen in Figure 5.6. It can be seen that the higher the pressure is, the harder it is for the SMP to expand and recover its original shape. Drawing a line of best fit, a linear correlation can be calculated for such behavior. At atmospheric conditions, maximum recovery occurs.

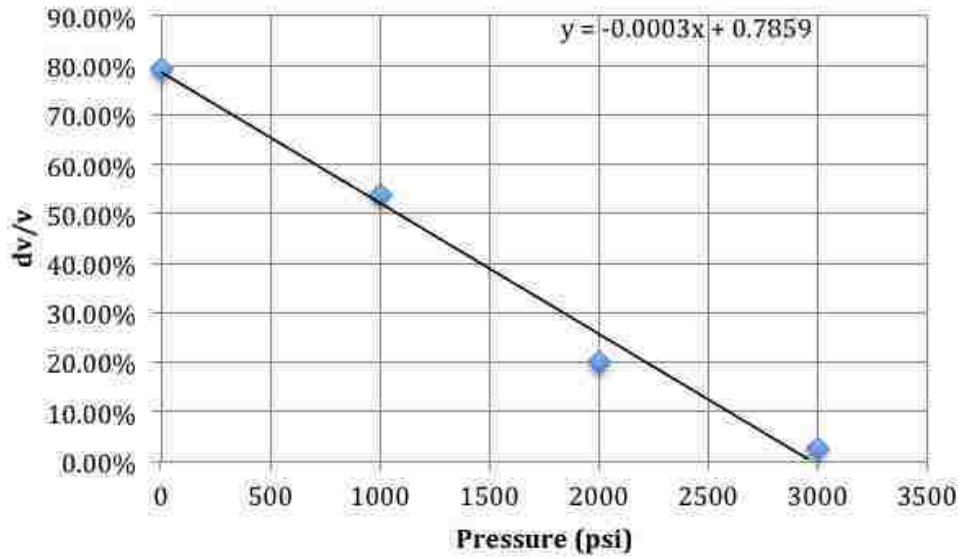

Figure 5.6. Change in volume of smart LCM versus pressure

5.1.4 Permeability Plugging Test

The objective of this test is to measure the sealing efficiency of the smart LCM at 80℃ and 23℃ with respect to time and compare the results. This experiment will help drilling engineers understand the difference between the smart LCM and a normal LCM that has no expansive properties. Table 5.3 shows the test parameters. The smart LCMs had an average diameter size of 5.87mm and an average thickness size of 1.63mm. The LCMs were added to 170 ml of mud at a concentration of 0.3 ppg. The mixture was then placed in the PPA Cell. Only a slot disc was used and it was placed on top of the PPA cell. The LCM receiver was then tightly capped to the PPA cell and the hydraulic pump was attached. The thermostat was then adjusted to 80℃ and the

mixture was left to settle at this temperature for 30 minutes. After that, oil was pumped from the hydraulic pump at a rate of 1 stroke per 10 seconds.

Table 5.3. Test Parameters

	Test 1 @80℃	Test 2 @23℃	Test 3 @23℃
Average Particle Diameter Size (mm)	5.87	5.87	5.48
Average Particle Thickness size (mm)	1.63	1.63	1.87

Every 30 seconds, the fluid loss and the pressure that the seal can hold were recorded as seen in Figure 5.7. The pressure reached to 3000 psi and was not allowed to exceed it.

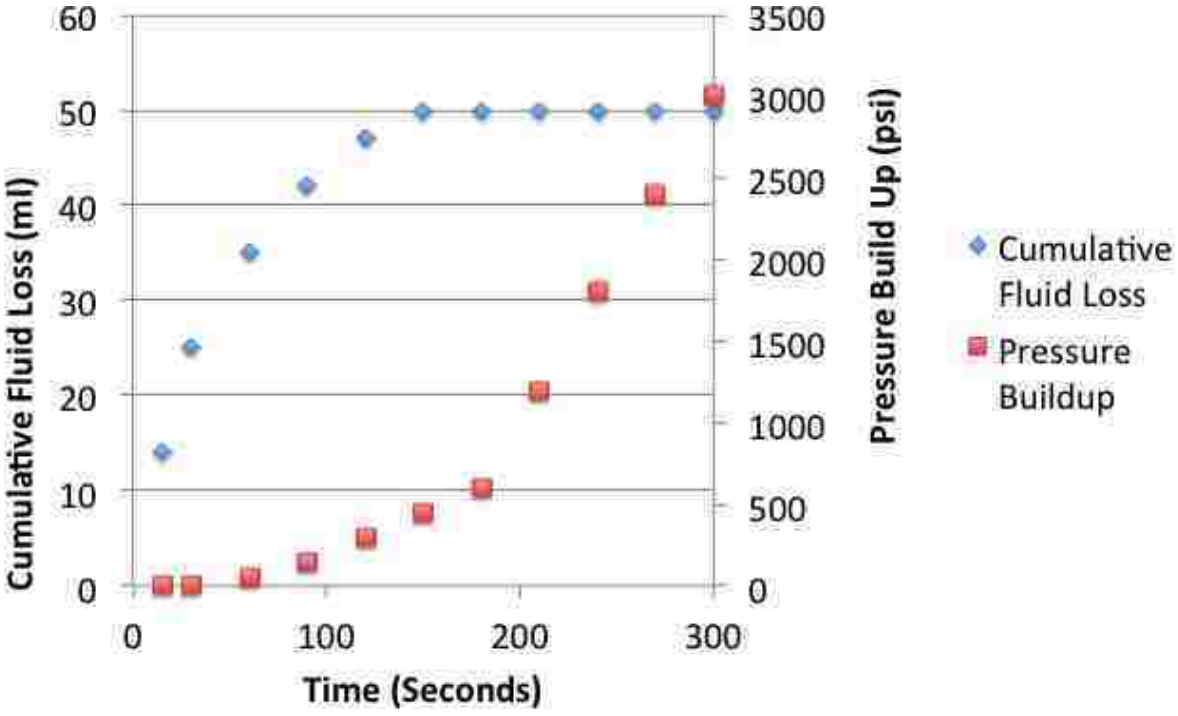

Figure 4.7. Fluid loss and pressure buildup at 80℃

From Figure 5.6, it is known that the particles expand by about 3% when the pressure is 3000 psi. Therefore, to understand if these particles can plug the fracture below activation temperature (23℃), two experiments were made. The first experiment was to see if the particles at a non-expanded size of 5.87 mm diameter and 1.63 mm thickness can seal the fracture alone without expanding and without needing temperature to activate them. For the second test, assuming that the only reason the smart LCMs sealed the particles was because they expanded in size, the expanded size of the LCM (5.48 mm diameter size and 1.87 mm thickness at room temperature) were mixed with the mud and tested to see if it will plug the fracture. Figure 5.8 and Figure 5.9 shows the results of these two tests.

It can be seen from the results that it is not only the expansive property that the LCM has that allows it to seal the fracture. What makes the smart LCM an excellent choice for sealing fractures is that it has the ability to take the shape of the fracture by bridging and sticking together. The cohesive property of this material allows it to withstand extremely high pressures.

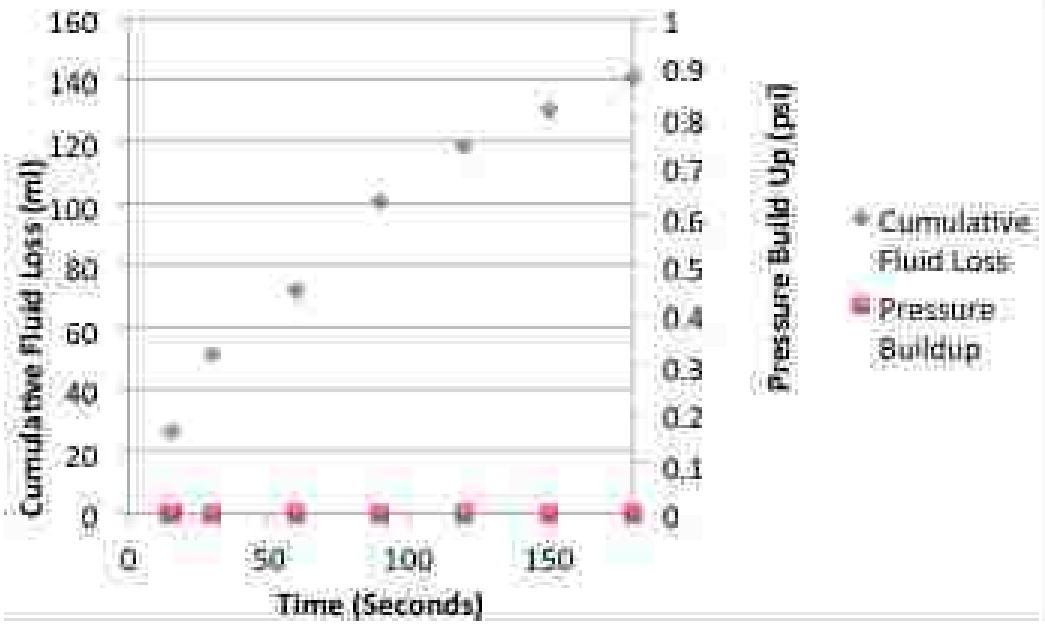

Figure 5.8. Results for normal size non-activated LCM @23℃

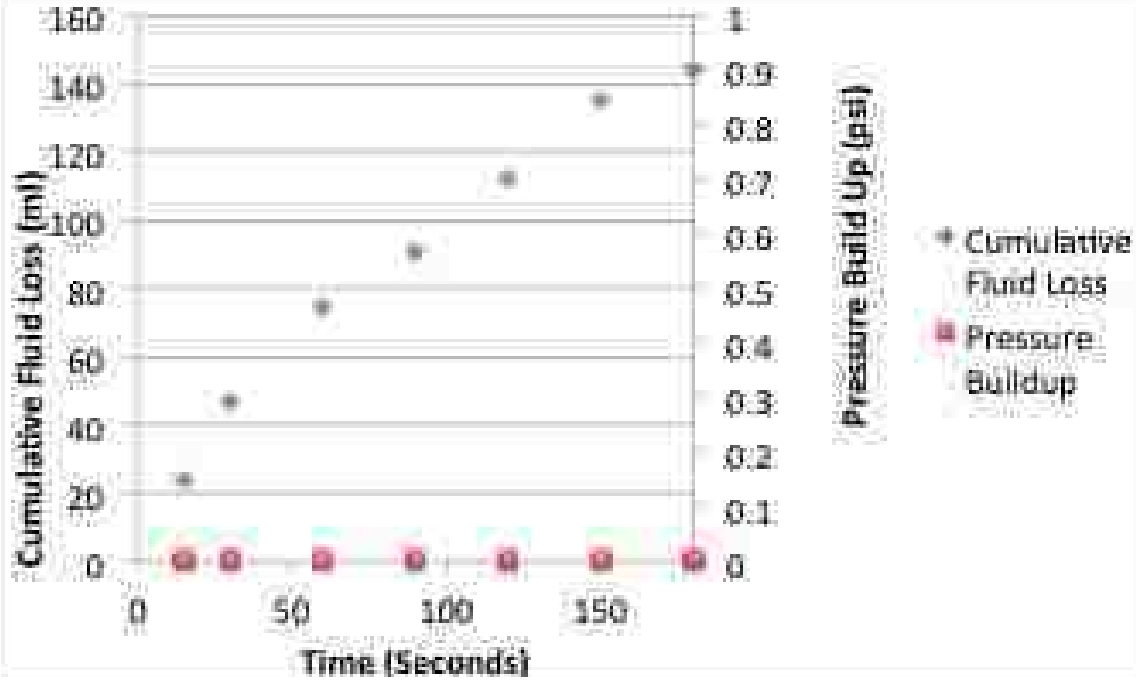

Figure 5.9. Results for expanded size non-activated LCM @23℃

5.1.5 Concentration Required for Sealing

The objective of this experiment is to test different concentrations of LCMs through the slot and tapered disc and see how much LCM is required to seal the fracture efficiently. The LCM particles used here had a shape of a thin sheet as opposed to disc shape in previous experiments. They were also much smaller in size ranging from 0.25mm to 1mm. They are made out of the same material but they have a different shape. So another objective of this experiment is to see if the shape of the material matters when trying to seal the fracture. The difference between LCMs shape can be seen in Figure 5.10.

These smart LCMs were mixed with 170 ml of the drilling fluid at concentrations of 0.24 lb/gal, 0.48 lb/gal and 0.96 lb/gal with the slot disc and the tapered disc. The heating jacket was set to a temperature of 85℃ and the mixture was left there to settle for 30 minutes before running the test.

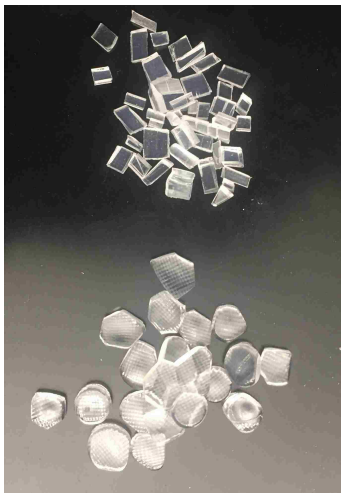

Figure 5.10. LCMs used in this experiment (top) vs. LCMs used in previous experiments (bottom)

Figure 5.11 and Figure 5.12 shows the fluid loss versus time and the pressure buildup versus time for the slot disc at each concentration respectively. It can be seen that as the concentration increases fluid loss does decrease but not by a large amount. The pressure that the seal can hold was also not very high as opposed to previous experiments.

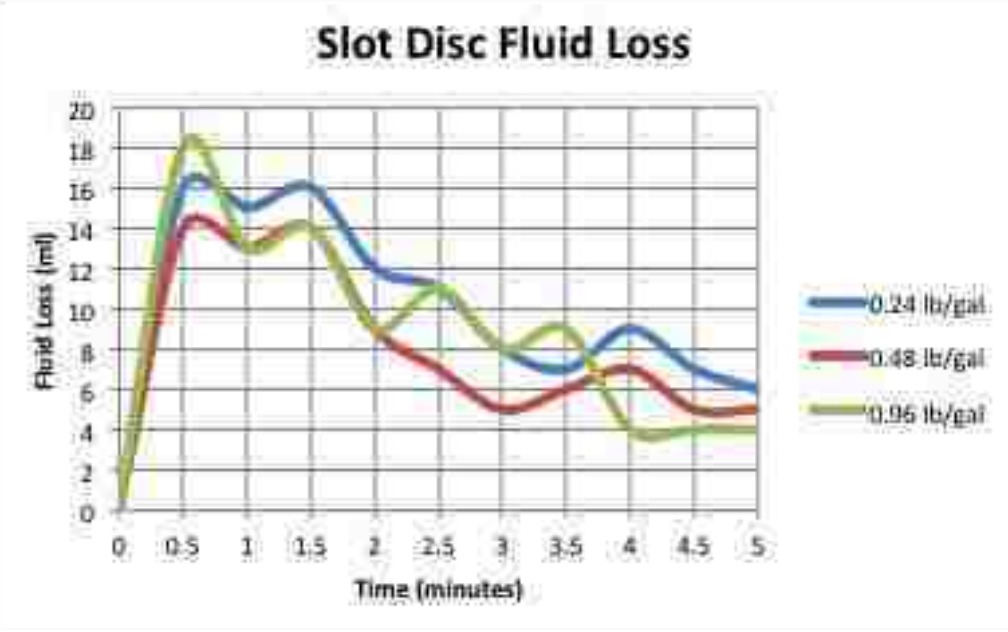

Figure 5.11. Fluid loss versus time for slot disc

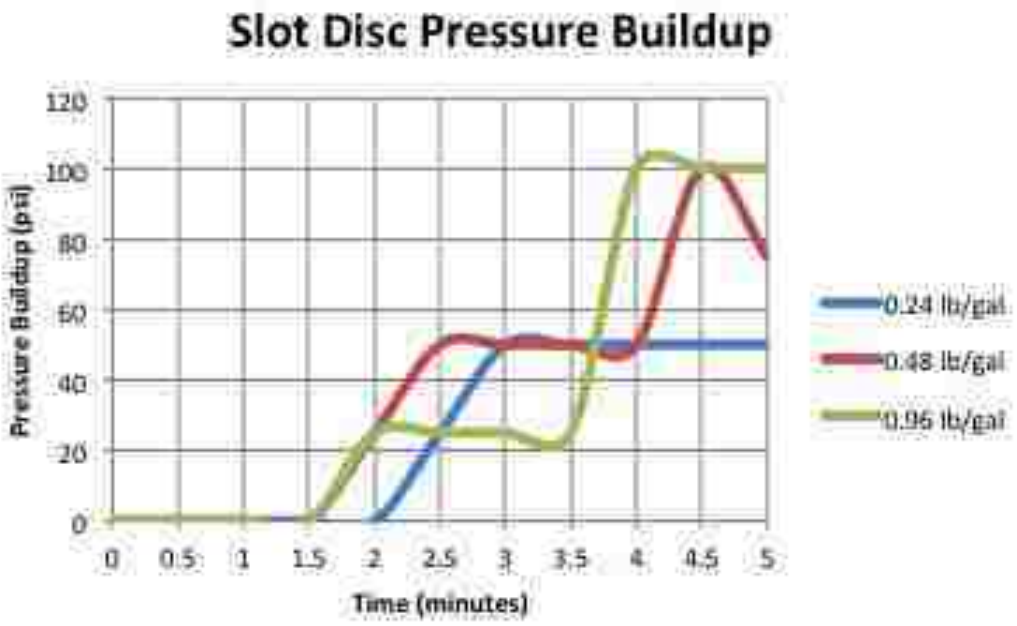

Figure 5.12. Pressure buildup versus time for slot disc

Figure 5.13 shows the slot disc sealed at two different concentrations. It can be seen that as the concentration increases, particles start to buildup beneath the actual fracture and form bridges within each other.

Figure 5.13. Slot disc sealed with 0.24 lb/gal of LCMs (top) versus 0.48 lb/gal bottom

Figure 5.14 and Figure 5.15 shows the fluid loss versus time and the pressure buildup versus time for the tapered disc at each concentration respectively. It can be seen that fluid loss decreases with increasing concentration and the pressure that the seal can hold increases with increasing concentration. However, the particles here caused a higher pressure buildup than in the slot disc. The particles tend to cause lower fluid losses and higher pressure buildups when the fracture is long in length as opposed to short in length.

The concentration of the LCMs and their shape can therefore have an effect on the effectiveness the smart LCMs' seal. The bridges that this shape formed were not as strong as the bridges that the disc shapes formed. Even though the pressure buildups were not as high as the previous experiments that used 3 lb/gal for concentration of LCMs, they still show a decrease in fluid loss and were able to withstand a reasonable differential pressure that will be seen in the wellbore whenever it is in an overbalance state.

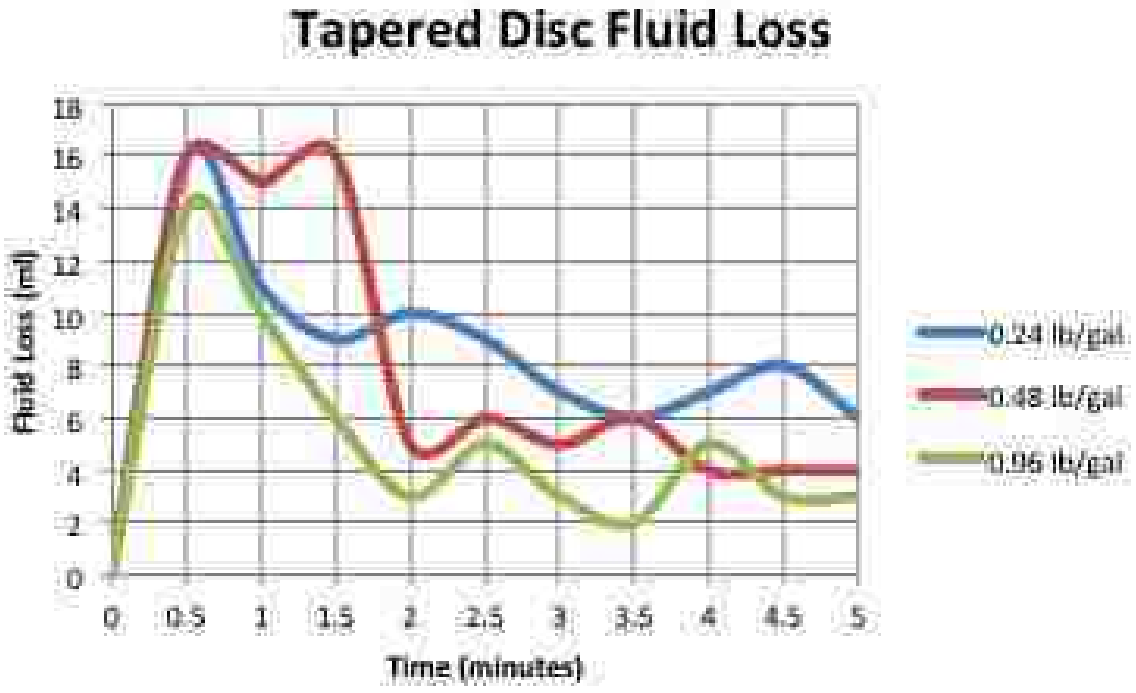

Figure 5.14. Fluid loss versus time for tapered disc

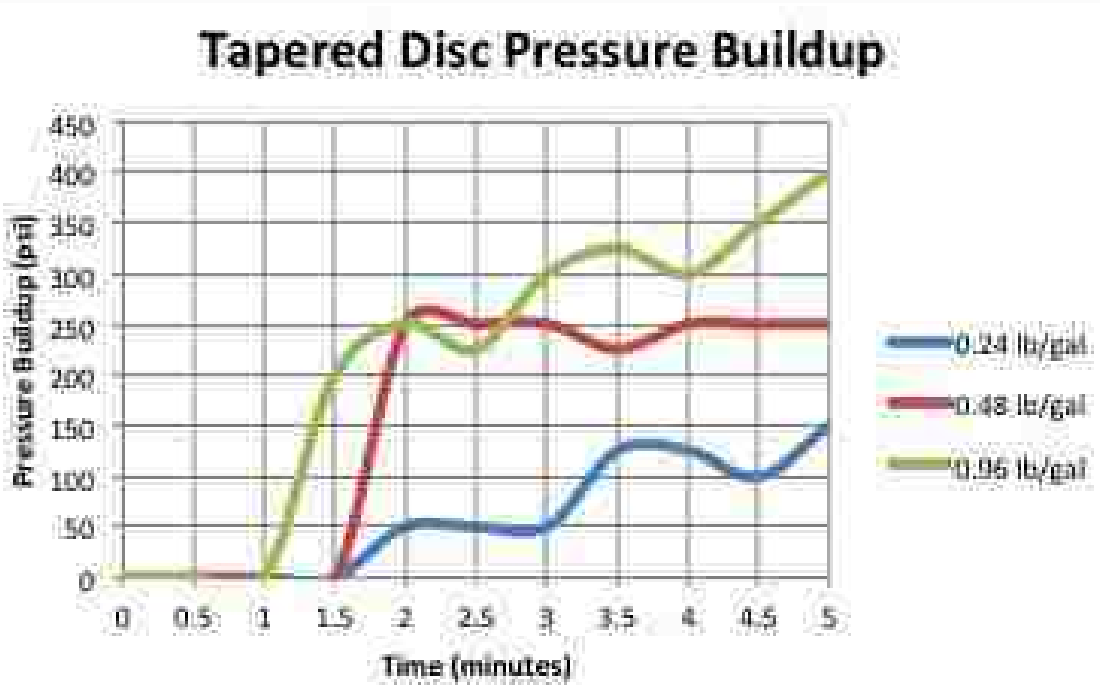

Figure 5.15. Pressure buildup for tapered disc

5.2 Numerical Simulation Results and Discussions

This section explains the numerical simulations made using the CFD-DEM coupling and the results obtained. The objective of the simulation is to test for the sealing efficiency of the smart LCMs by measuring fluid loss, estimate the concentration of particles required for fracture sealing (one-size particles or a mixture of sizes) and finally, measure the overall stress recovery of the smart LCM.

5.2.1 Simulation Validation

The objective of this simulation is to validate that the results from the simulation are correct and match the experimental results from Chapter 5.1.2. For this simulation, the particle undergoes thermal expansion and since the seal was withstanding up to 5000 psi in the experiment, the particles are only allowed to expand by up to 3% according to the strain expansion measurement test.

The seal made by the particles and the change in volume from the particles' expansion can be seen in Figure 5.16.

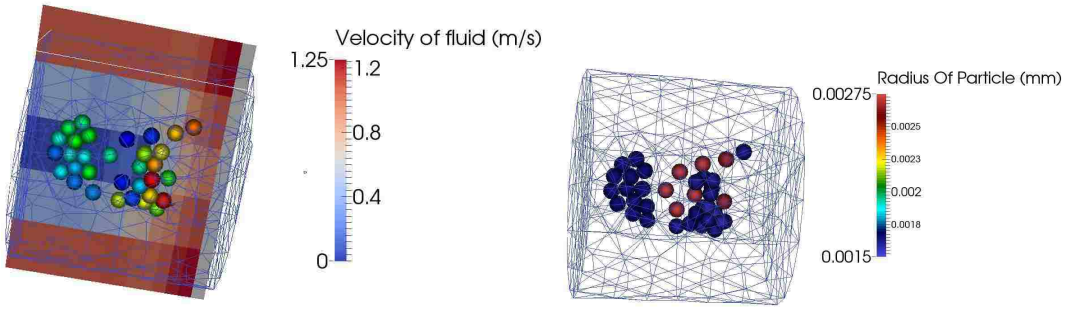

Figure 5.16. Sealing of tapered disc in the simulation

Figure 5.17 shows the comparison between the concentration required to seal the fracture in the experiment and the concentration required to seal the fracture in the simulation. It can be seen that they are very similar.

Figure 5.18 shows the comparison of the fluid loss versus time between the experiment and the simulation. Figure 5.19 shows the comparison of the pressure build-up versus time between the experiment and simulation. Both of Figure 5.18 and Figure 5.19 show that the results are matching for both the simulation and the experiment. The simulation can be trusted to generate results for a new sized fracture. The simulation was also repeated with particles that did not have any expansive or cohesive properties. This simulation was made for comparison with results from Chapter 5.1.4. It was seen that these particles failed to seal the tapered disc and they were not able to minimize fluid loss.

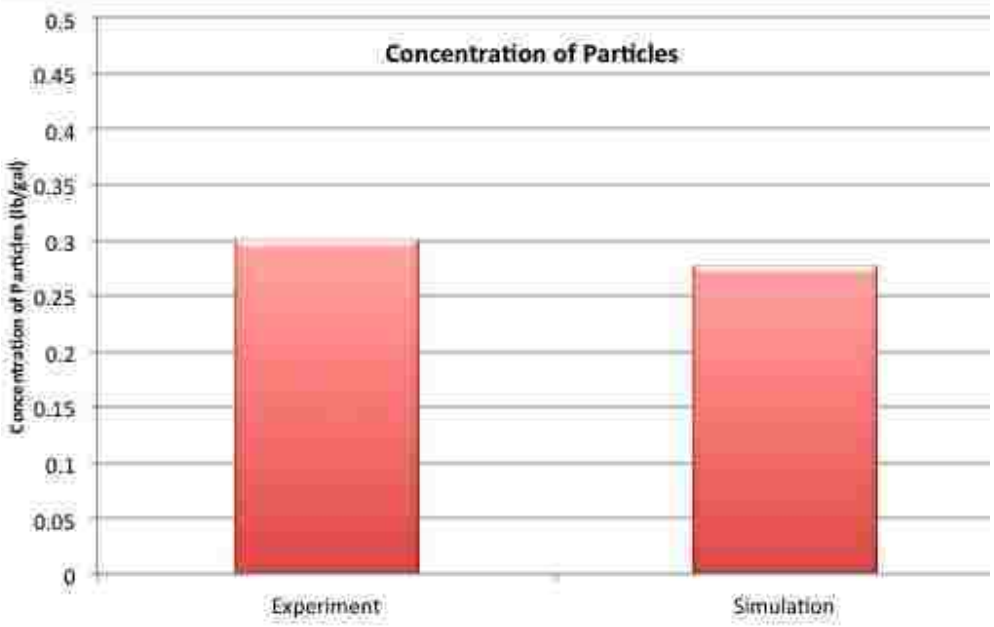

Figure 5.17. Concentration of particles comparison

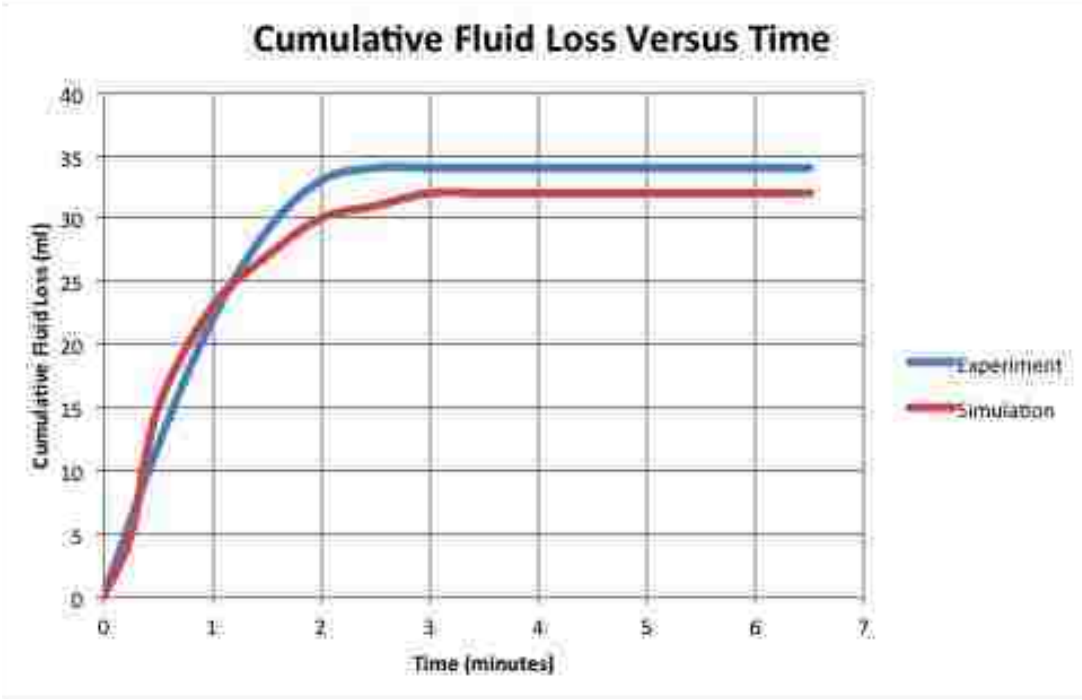

Figure 5.18. Cumulative fluid loss comparison

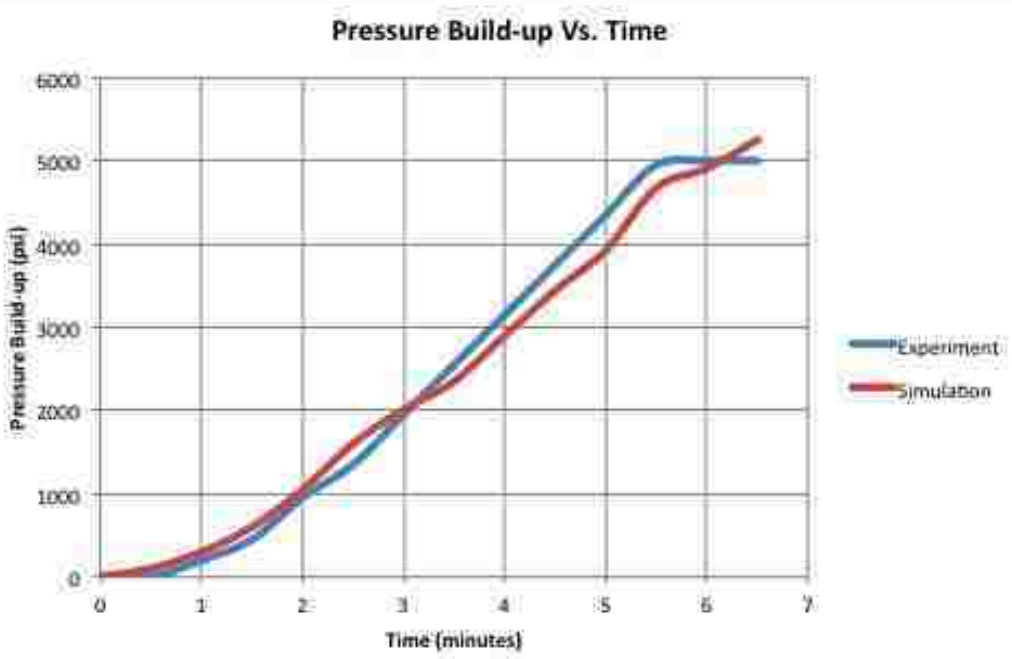

Figure 5.19. Pressure build-up comparison

5.2.2 Cumulative Fluid Loss

The objective of this simulation is to see how effective the smart LCMs are at sealing the fracture by comparing different particle sizes and mixed size distributions. This simulation extends the work done in the experiments using a different fracture size. For this simulation, the particle undergoes thermal expansion. The maximum volumetric strain allowed is the strain measured in strain expansion measurement test in Chapter 5.1.3. From this test and for one of the results, an arbitrary ΔT was chosen and the thermal coefficient was then calculated. ΔT was then changed for the other results to maintain the volumetric strain at each pressure. Table 5.4 shows the temperatures used, volumetric expansion allowed and radius expansion ($\frac{\Delta R}{R}$) for the spherically shaped particles at each inlet pressure. This expansion procedure was also used in Chapter 5.2.1.

Table 5.4. Thermal expansion for smart LCM

	1000 psi	2000 psi	3000 psi
$\frac{\Delta V}{V}$ (%)	55	18	3
$\frac{\Delta R}{R}$ (%)	16.5	5.5	1
α	0.00825	0.00825	0.00825
ΔT (°C)	20	7	2

The cumulative fluid loss versus time at 1000 psi for the 2mm particles was one of the data measured and can be seen in Figure 5.20. It can be seen that at about 3 minutes the particles have been fully activated and were big enough to form a tight seal that prevented the fluid from being lost. Figure 5.21 shows the temperature of the fluid at the beginning and at the end of the simulation. This increase in temperature is what caused the activation. Fluid loss was high at the beginning since the smart LCMs were still in the process of activation.

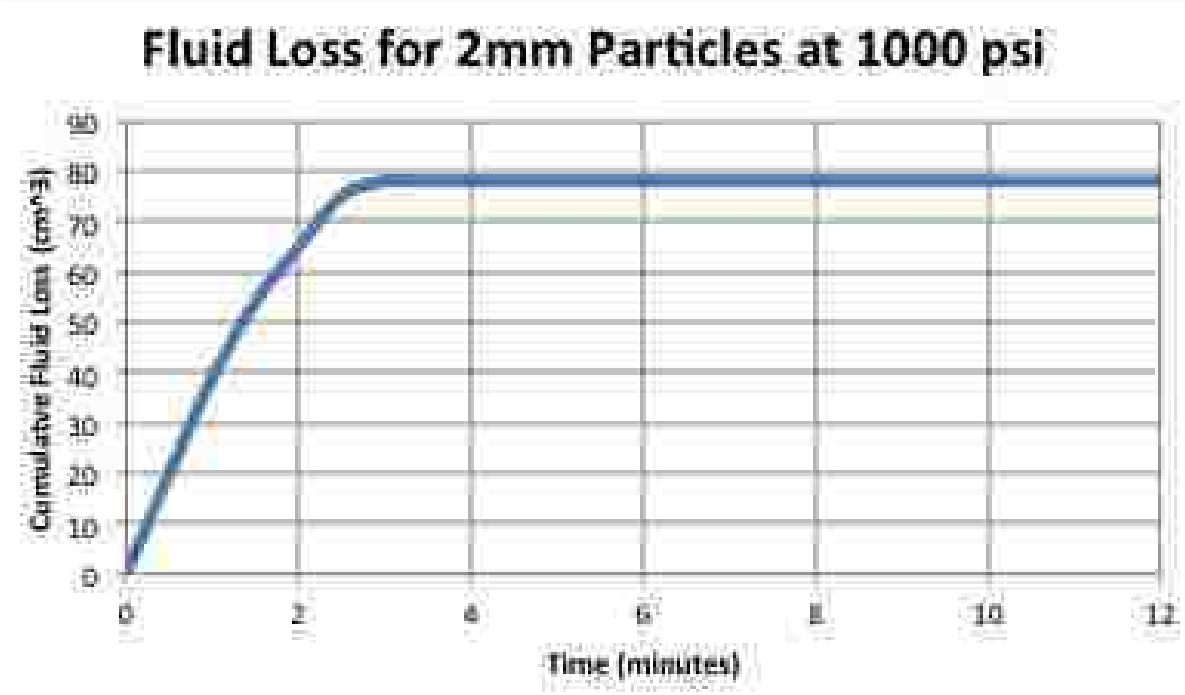

Figure 5.20. Fluid loss for 2mm particles at 1000 psi

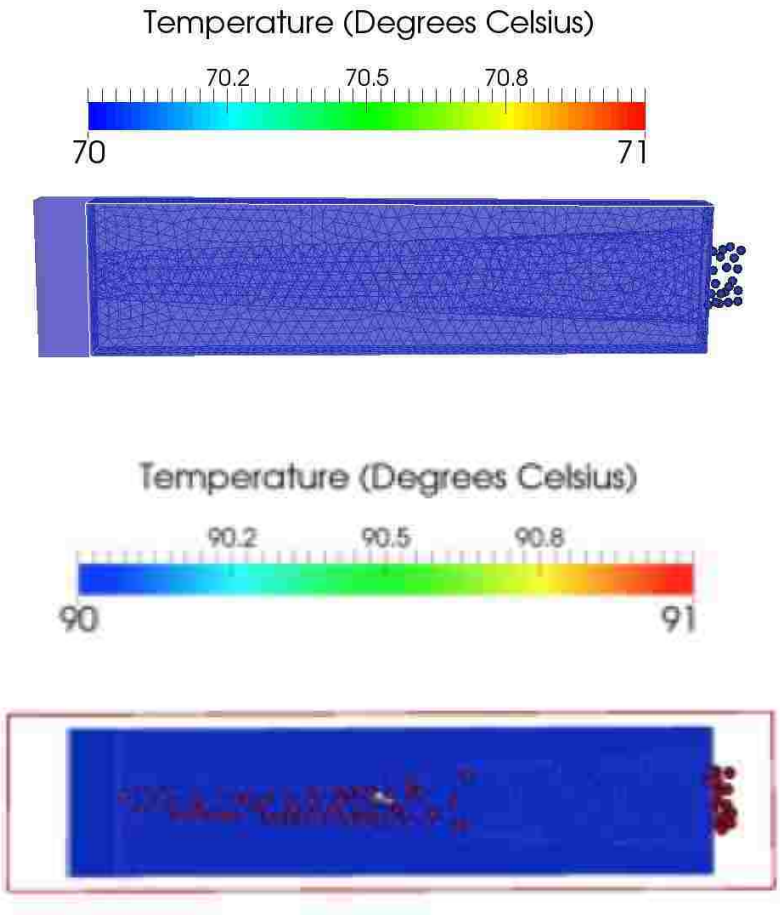

Figure 5.21. Temperature of fluid before (top) and after (bottom) activation

The fracture was efficiently sealed and the velocity of the fluid before and after was recorded as seen in Figure 5.22. The velocity decreased after the fracture got plugged.

Table 5.5 shows the cumulative losses for each particle size at each pressure. It can be seen that as the particles increase in size, fluid loss decreases. Fluid loss increases when pressure increases because the particle sizes are expanding in smaller amounts as opposed to expansions in lower pressures. Therefore, this decrease in size requires more LCMs and it takes more time for the fracture to be sealed. This extra time required accounts for more fluid loss. However, it was seen that all smart LCMs were able to seal the fracture effectively and stop any further losses.

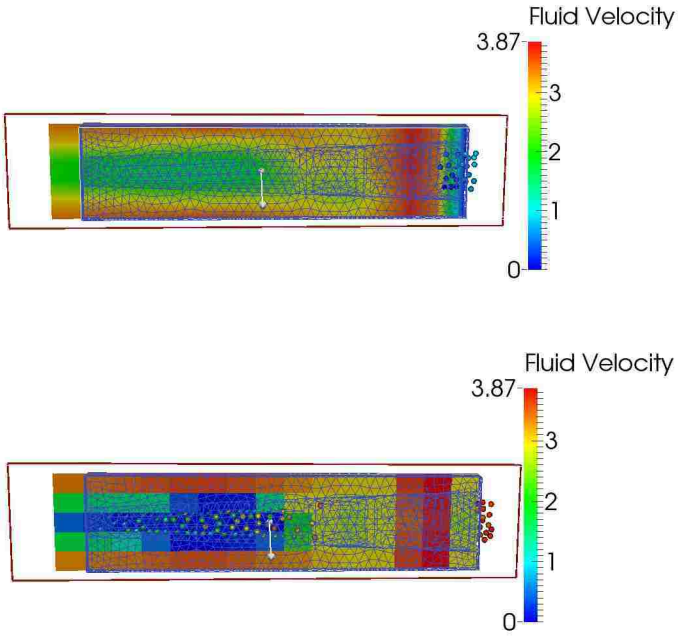

Figure 5.22.Velocity of fluid in m/s before (top) and after (bottom) plugging

Table 5.5. Cumulative fluid loss for each particle size at different inlet pressures

	1000 Psi	2000 psi	3000 psi
1.25mm	158 cc	197 cc	220 cc
1.5mm	128 cc	169 cc	181 cc
2mm	79 cc	94 cc	122 cc
2.5mm	22 cc	46 cc	67 cc

The cumulative fluid loss for the mixture of 1.25mm and 2mm particle sizes versus time at 1000 psi can be seen in Figure 5.23. It can be seen that the fluid loss is decreasing with time and the total fluid loss for the mixed particle sizes is less than having a 2mm particle size by itself or a 1.25 mm particle size by itself. It can also be seen that it takes less time for the mixture to stop fluid losses than it does for having just one sized particle. Table 5.6 shows the cumulative fluid losses for the mixture at each pressure.

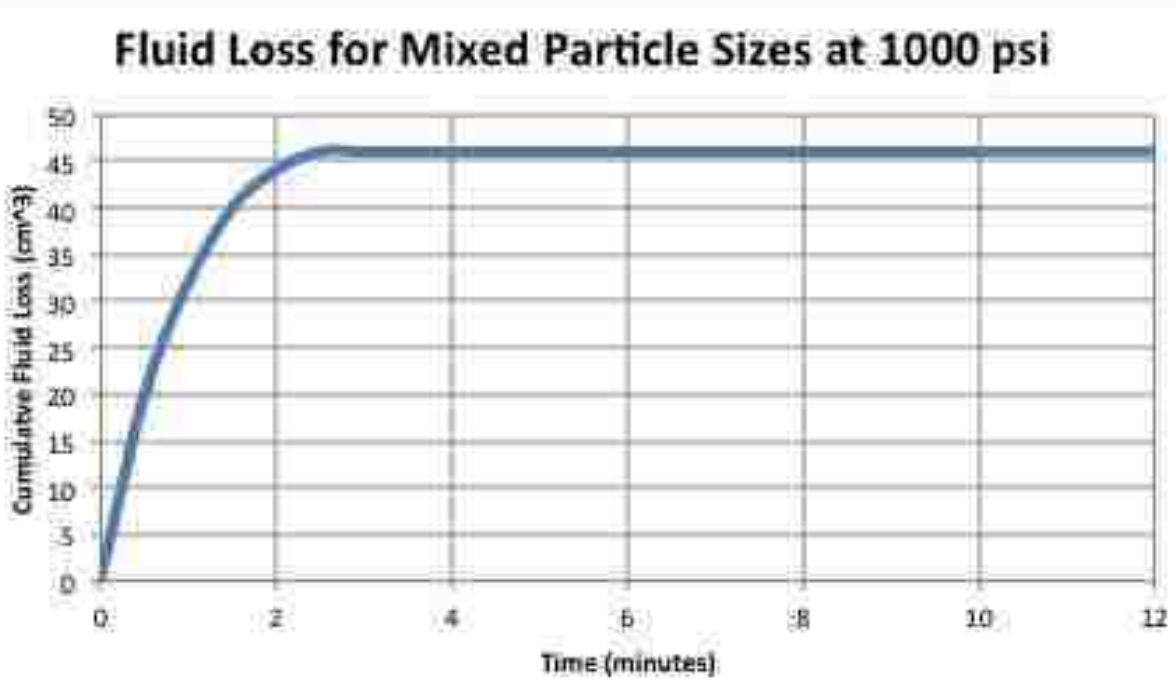

Figure 5.23. Cumulative fluid loss versus time for the mixed particles (1.5mm and 2mm) at 2000 psi

Table 5.6. Cumulative fluid loss for the mixed particle sizes at each pressure

	1000 Psi	2000 psi	3000 psi
Mixture of 1.25mm and 2mm	47 cc	83 cc	106 cc

Figure 5.24 compares the cumulative fluid losses for each particle size and for the mixture. It can be seen that the mixture of particles is much better at sealing the fracture than having one-sized particles. This can be explained by how the mixed particles were packed compared to the packing of the single sized particles.

Figure 5.25 shows the porosity of the mixture of particle sizes compared to the porosity of only 2mm particles at 1000 psi. It can be seen that the porosity is extremely small in the mixture due to better packing between the particle sizes and therefore, it is much harder for the fluid to pass as opposed to the porosity and packing in the 2mm particles.

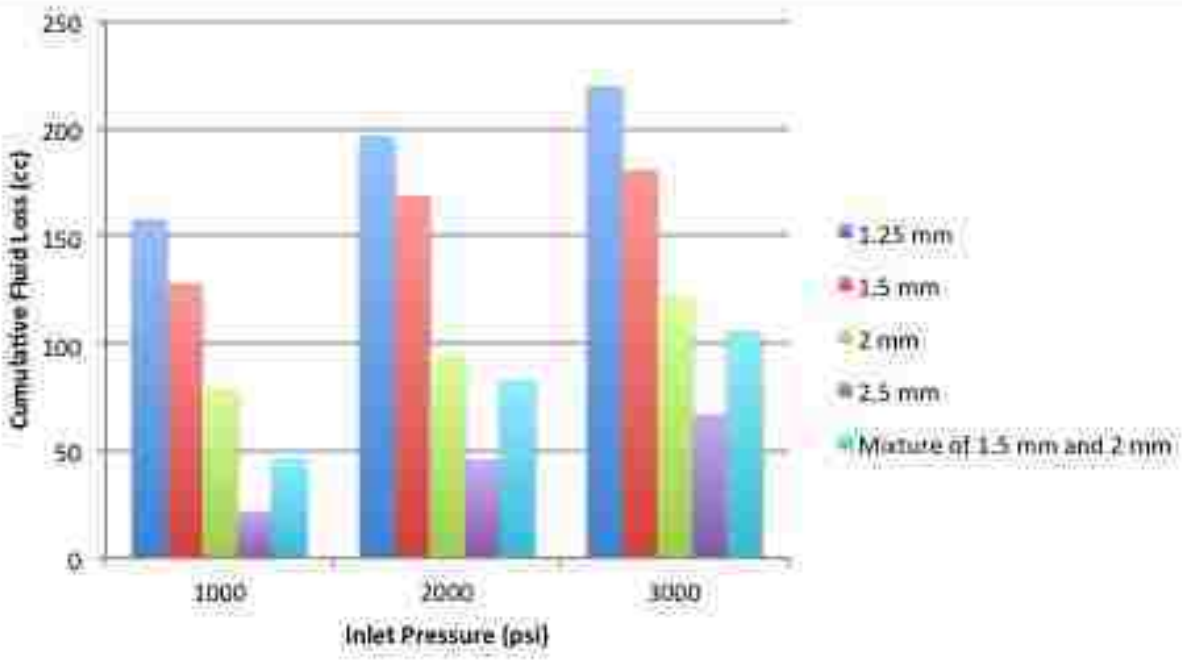

Figure 5.24. Comparison of cumulative fluid loss for each particle and mixture

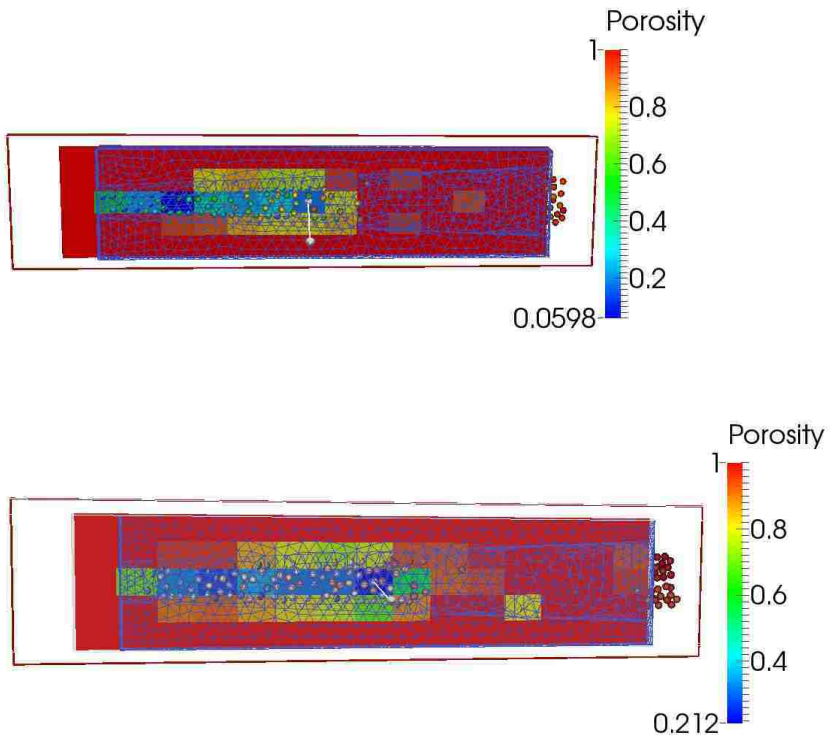

Figure 5.25. Porosity and packing of mixed particles (top) versus 2mm particles (bottom)

5.2.3 Concentration of Particles Required to Seal the Fracture

The objective of this simulation is to measure the number of particles required to plug the fracture. This was made by measuring the concentration of smart LCMs needed to bring fluid loss to less than 3 cm^3/min in Chapter 5.2.1.

At 1000 psi, 142 particles of 2mm radius size were required to efficiently seal the fracture and prevent fluid loss as seen in Figure 5.26. Which means that for this fracture shape, a concentration of 0.195 lb/gal of 2mm smart LCMs is required to seal it.

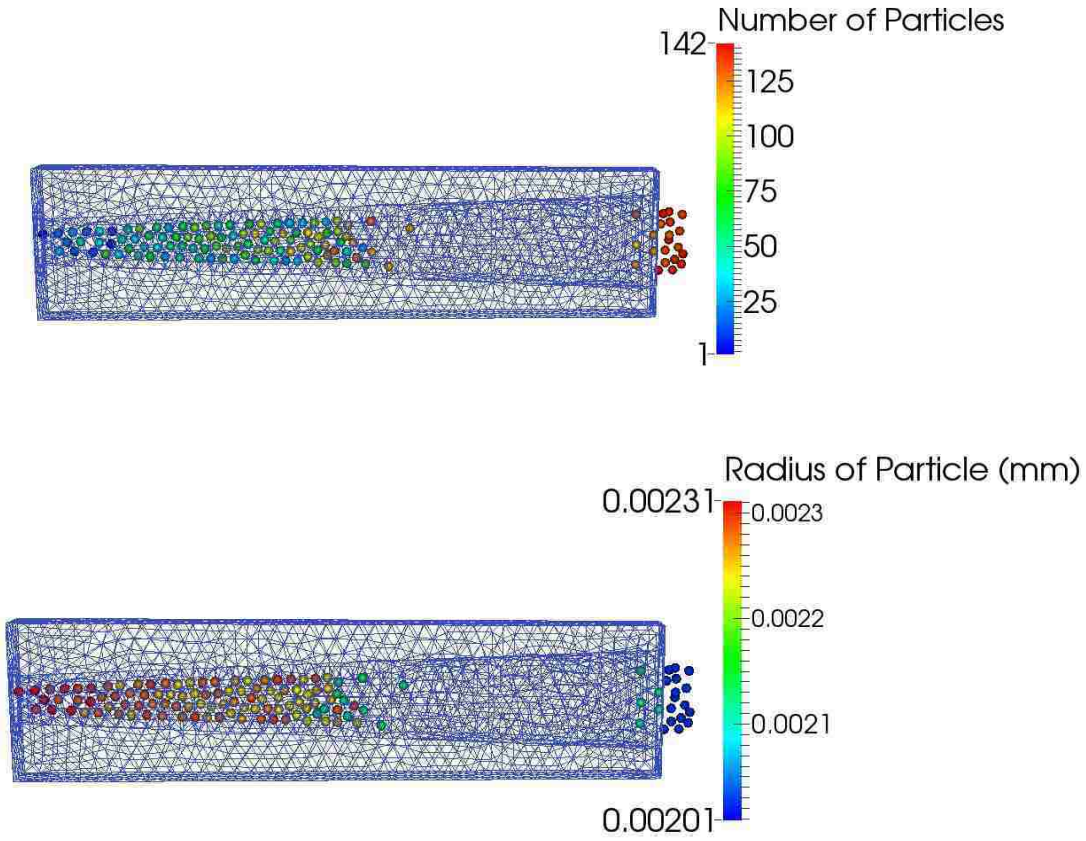

Figure 5.26. Number of 2mm particles required for plugging a fracture at 2000 psi.

The concentration of particles in pounds per gallon for each size at each pressure required to plug the fracture can be seen in Figure 5.27. It can be seen that as the particles increase in size,

the concentration of particles required to seal the fracture decreases. It can also be seen that as the pressure increases more particles are required to seal the fracture and this is because the particles expand by less due to higher pressures and therefore, more particles are required to effectively seal the fracture.

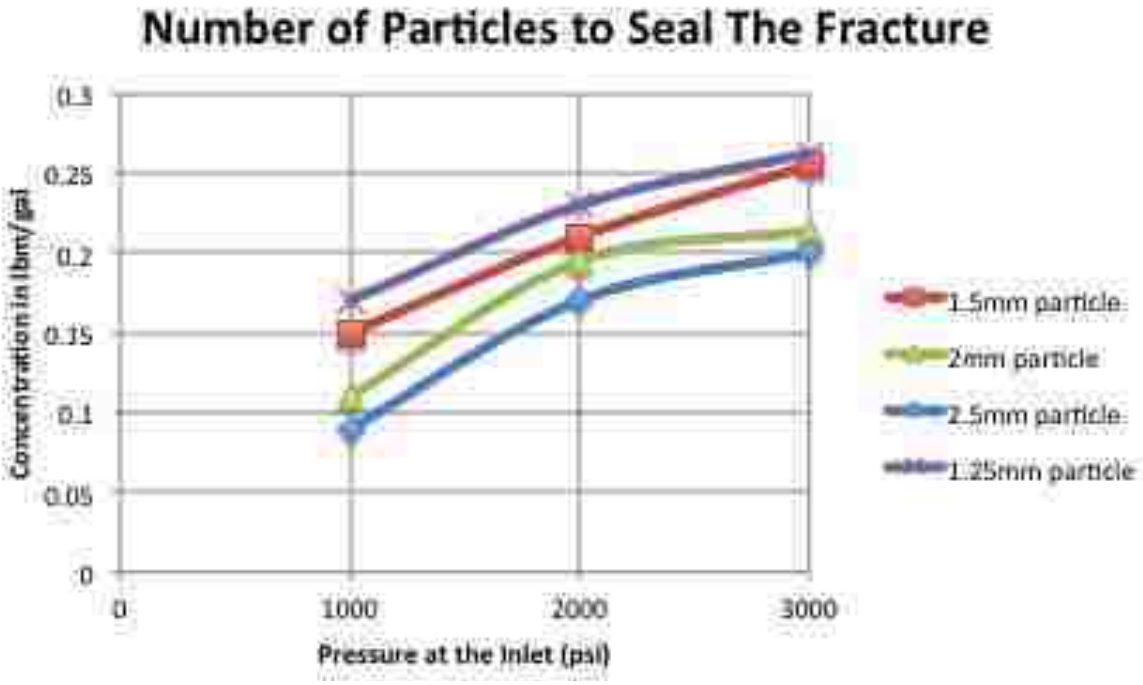

Figure 5.27. Number of particles required to seal the fracture.

For the mixed particles, the number required to seal the fracture at 1000 psi was a total of 220 from which 110 particles were 2 mm size and 110 particles were 1.5 mm size as seen in Figure 5.28. Which means that for this fracture, a concentration of 0.22 lb/gal of 2mm and 1.5mm smart LCMs is required to seal it.

The concentration of particles for this mixture required to plug the fracture at each pressure can be seen in Figure 5.29. It can be seen that the concentration of smart LCMs increase with increasing pressure. However, less particles of each size are required to seal the fracture at a given pressure when in a mixture compared to single sized particles.

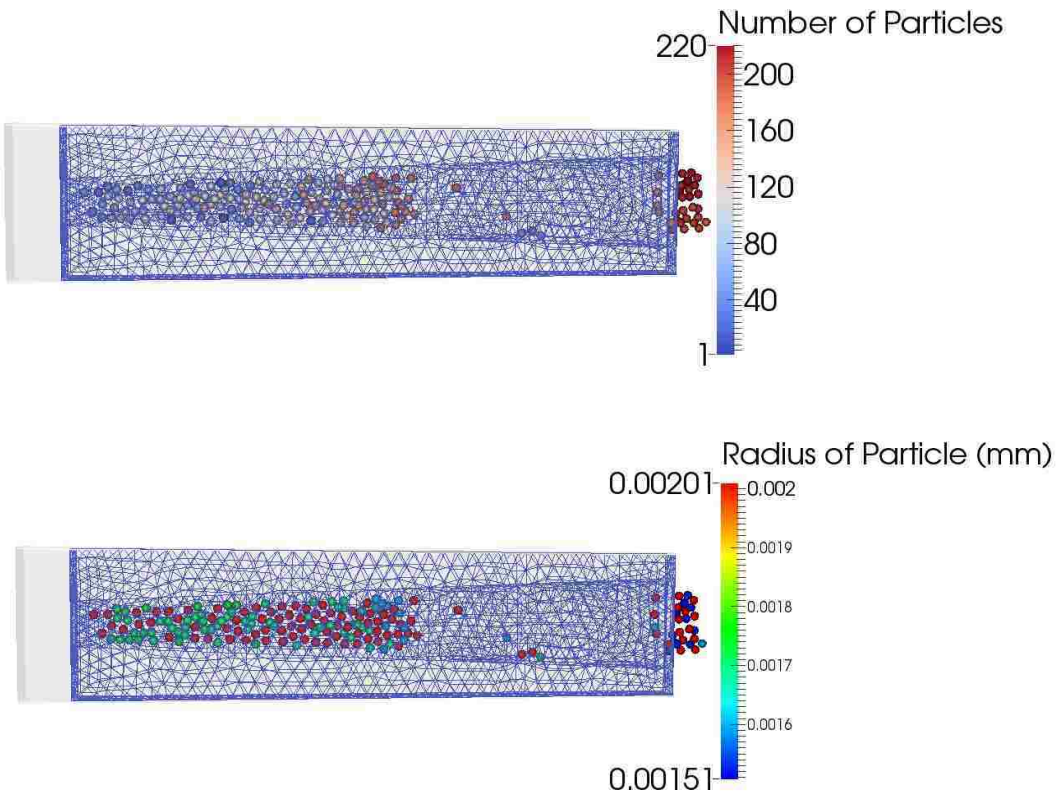

Figure 5.28. Mixture of 1.5mm and 2mm (ratio 1:1) particles at 1000 psi

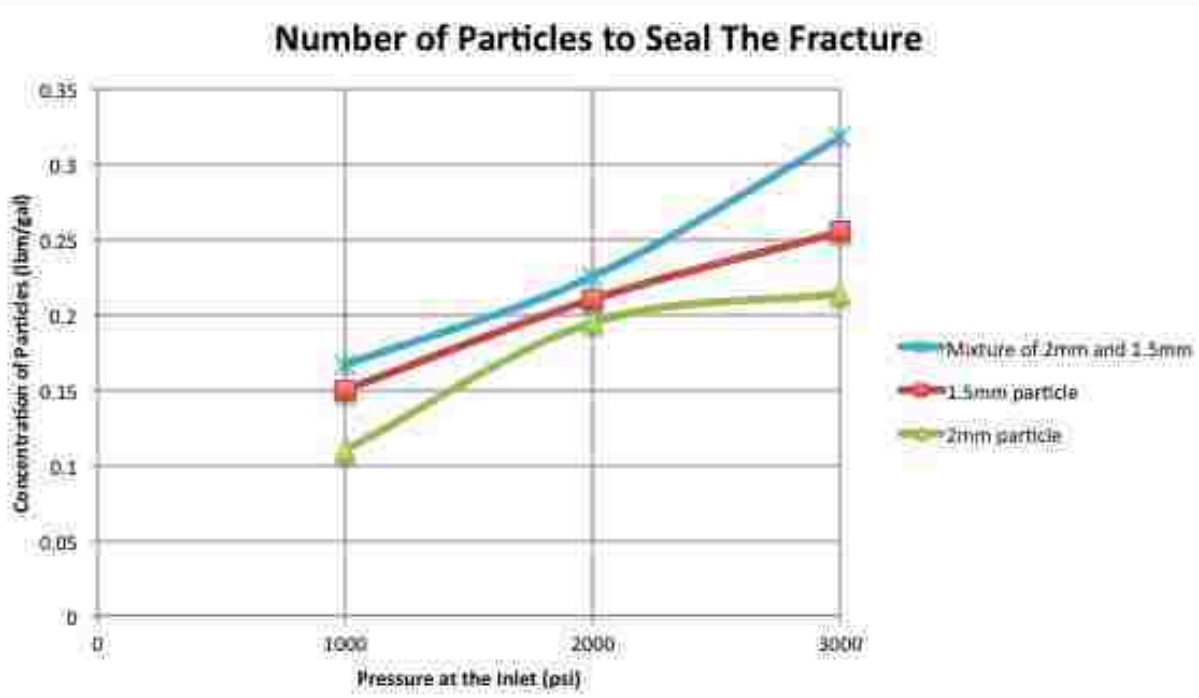

Figure 5.29. Number of mixed particles (1.5mm and 2mm) to seal the fracture

5.2.4 Stress Recovery of Smart LCM

The objective of this simulation is to calculate the stress recovery during shape transformation of the smart LCMs. The stress was calculated in the simulation using Equations 2.15-2.17. The strain values are given from the experimental strain measurement test. The input parameters for the simulation can be seen in Table 5.7 and they are based on the material properties and the results in the experiment. The material here is a perfect sphere and is considered elastically isotropic. The radius is the only variable that changes and leads to the volumetric expansion calculated in the experiment.

Table 5.7. Input parameters for recovered stress

	0 psi	1000 psi	2000 psi	3000 psi
ε_s	0.79	0.79	0.79	0.79
ε_{pre}	0.25	0.25	0.25	0.25
E_i (MPa)	260	260	260	260
E_e (MPa)	2.4	2.4	2.4	2.4
$\frac{\Delta V}{V}$ (from experiment)	0.79	0.55	0.18	0.03
ε-$\int_{T_h}^{T} \alpha dT$ (from experiment)	0.23	0.165	0.055	0.01

The overall recovery stress that the particles apply on walls of the fracture at 1000 psi was 1.77 MPa as seen in Figure 5.26.

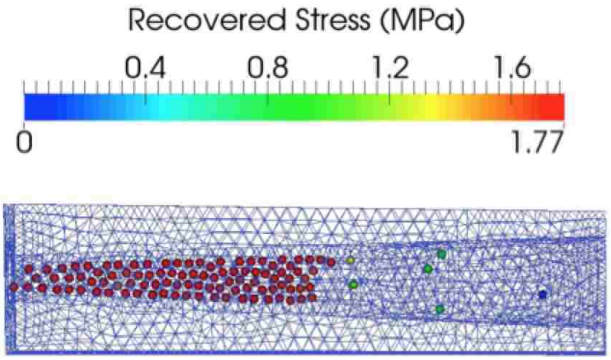

Figure 5.30. Recovery stress of the smart LCMs at 1000 psi

It can be seen that stress recovered is considerably high and could therefore, help strengthen the wellbore. Figure 5.27 shows the stresses at each inlet pressure for the 2mm particle. The stresses increase with increasing pressure and this is because the smart LCM's strain recovery is limited due to the confined environment and is transformed to recovered stress.

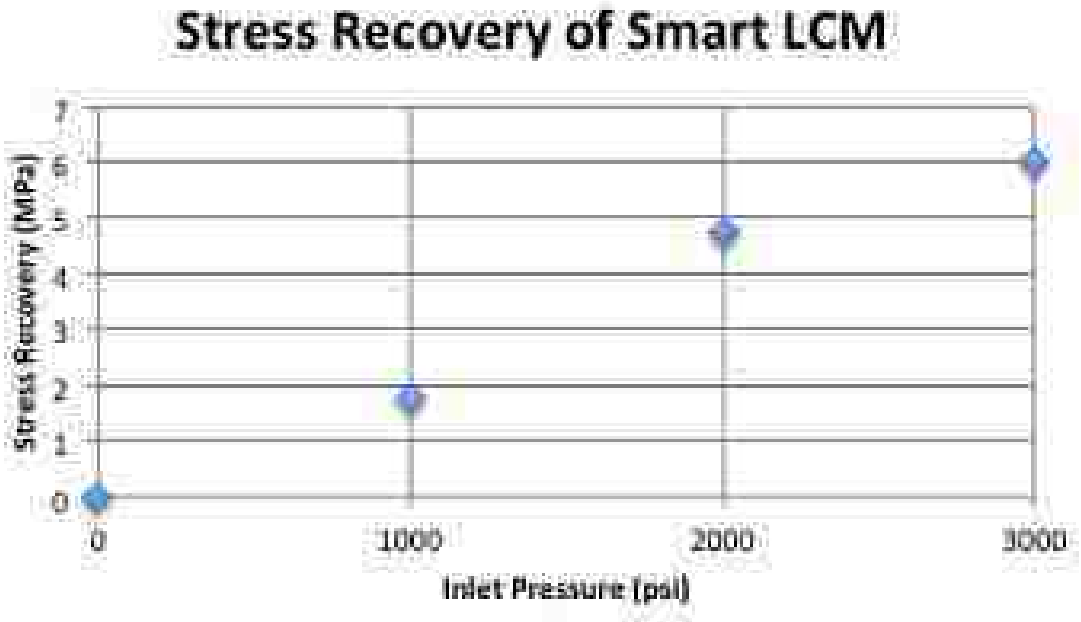

Figure 5.31. Recovery stress of smart LCM

Chapter 6: Conclusions and Recommendations for Future Work

To reduce or prevent fluid loss and strengthen the wellbore, a new type of smart expandable lost circulation material is introduced in this research. The smart expandable LCM was tested experimentally via permeability plugging apparatus to evaluate the LCM's sealing efficiency. A fully coupled CFD-DEM model was also built to measure the cumulative fluid loss, concentration required to seal the fracture and the recovered stress that will act on the wellbore wall due to the shape deformation of the smart LCM. The main parameters considered in this study were LCM size, various temperatures including LCM activation temperature and various confining bottomhole pressures.

The expansive properties of the proposed LCM makes it an effective solution not only in bridging and sealing vugs and fractures but also inducing compressive stresses to strengthen the wellbore without damaging the reservoir permeability. It was seen that temperature plays an important role in impacting the performance of LCM as it gets activated above a specific temperature. For instance, at 60°C, the smart LCM is beneath activation temperature and can't seal the fracture as opposed to 80°C where it was activated and the fracture was effectively sealed. This seal is also able to withstand up to 5000 psi differential pressure without breaking. The smart LCMs have the ability to stick together and bridge effectively when activated and that gives it an advantage above other types of LCMs. It was also seen that confining pressure strongly affects the expansion of the smart LCM. The higher the confining pressure, the less expansion the smart LCM shows. However, as the expansion decreased, the recovered stress increased. The smart LCM's recovered stress reached up to 6 MPa. The concentration of the smart LCMs depends on the particle size and the confining pressure. Mixing particle sizes was seen to be one of the most efficient ways to seal a fracture due to the packing of the particles.

The experiment was limited to only static fluid loss and does not fully imitate the circulation in the wellbore. There were no bigger slot disc sizes available for testing and therefore, plugging of bigger fractures had to be simulated. Overall, the experimental and numerical simulation results were good which suggests that the material should be further investigated for a possibility to be implemented in the field. For instance, having such recovered stress could reduce the chances of the wellbore in going in tension and strengthen it. Also, the expansive and chemical properties of the LCM should allow it to fill the shape of the fracture and seal it even if it has a big shape. Improvements in the experiments and the numerical model, as well as recommendations for future work include

1. Measure the three different components of stress (memorized stress, relaxed stress and thermal stress) that are released from the smart LCM. This could be done by performing lab experiments using dynamic mechanical analysis tester and using the values collected to construct a MATLAB code using the equation in chapter 2.6.
2. Further recommendations for the experimental tests are

a) Investigation of smart LCMs with different activation temperatures to see if there is a link between activation temperature and sealing efficiency.
b) Measure the strain volume changes for another type of smart LCM that has a different pre-strain value.
c) Testing more disc sizes to see how effective the smart LCM is at sealing bigger fracture sizes.

3. Further recommendations for the numerical simulations are

a) Test more mixed particle sizes in the CFD-DEM model to confirm that mixed particle sizes have better packing than single sized particles.

b) Test different mixed particle ratios using the bridging theories listed in the literature.

c) Test bigger sized fractures to confirm that the smart LCM can seal bigger fractures.

d) Vary the differential pressure between the inlet and the outlet and see if it affects concentration and fluid loss.

Bibliography

Aadnoy, B. S. and Belayneh, M. 2004: "Elasto-Plastic Fracturing Model for Wellbore Stability Using Non-Penetrating Fluids." Journal of Petroleum Science and Engineering, Vol. 45 (3), pp. 179-192.

Abrams, A. 1977: "Mud Design to Minimize Rock Impairment Due to Particle Invasion"

Adams, M. J., & Perchard, V.,1985: "The cohesive forces between particles with interstitial liquid." In *Institute of Chemical Engineering Symposium* (Vol. 91, pp. 147-160).

Al-saba, M. T., R. Nygaard, A. Saasen, and O. M. Nes, 2014: "Laboratory Evaluation of Sealing Wide Fractures Using Conventional Lost Circulation Materials," Paper SPE 170576, presented in SPE Annual Technical Conference and Exhibition, Society of Petroleum Engineers, Amsterdam, The Netherlands.

Al-saba, M. T., R. Nygaard, A. Saasen, and O. M. Nes, 2014: "Lost Circulation Materials Capability of Sealing Wide Fractures," Paper SPE 170285, presented in SPE Deepwater Drilling and Completions Conference, Society of Petroleum Engineers, Galveston, TX, USA.

Alberty, M. W. and McLean, M. R., 2004: "A Physical Model for Stress Cages." Paper SPE 90493, presented in SPE Annual Technical Conference and Exhibition, Houston, USA.

Arshad U, B. Jain, H. Pardawalla, N. Gupta and A. Meyer, 2014: "Engineered Fiber-Based Loss Circulation Control Pills to Successfully Combat Severe Loss Circulation Challenges During Drilling and Casing Cementing in Northern Pakistan," Paper SPE 169343, presented at the SPE Latin American and Caribbean Petroleum Engineering Conference, Society of Petroleum Engineers, Maracaibo, Venezuela.

Brandl, A., Bray, W. S., & Molaei, F., 2011: "Curing Lost Circulation Issues and Strengthening Weak Formations with a Sealing Fluid for Improved Zonal Isolation of Wellbores." Presented in Australian Geothermal Energy Conference, Melbourne.

Bruton, J. R., Ivan, C. D., and Heinz, T. J., 2001: "Lost Circulation Control: Evolving Techniques and Strategies to Reduce Downhole Mud Losses." Paper SPE 67735, presented in SPE/IADC Drilling Conference, Amsterdam, the Netherlands.

Cook J., F. Growcock, Q. Guo, M. Hodder and E. van Oort, 2012: "Stabilizing the Wellbore to Prevent Lost Circulation," Oilfield Review 23, no. 4, 26–35.

Cundall, P.A. and O.D.L. Strack. 1979: "A Discrete Numerical Model for Granular Assemblies". In: Geotechnique 29.1, pp. 47–65.

Deeg, W., and Wang, H. 2004: "Changing Borehole Geometry and Lost-Circulation Control." ARMA-04-577, the 6th North America Rock Mechanics Symposium, Houston, Texas, USA.

Di Felice, R. 1994: “The voidage function for fluid-particle interaction systems”. In: International Journal of Multiphase Flow 20.1, pp. 153–159. issn: 03019322. doi: 10.1016/0301-9322(94)90011-6.

Dupriest, F. E., 2005: “Fracture Closure Stress (FCS) and Lost Returns Practices.” Paper SPE 92192, presented in SPE/IADC Drilling Conference, Amsterdam, Netherlands.

Dupriest, F. E., Smith, M. V., Zeilinger, C. S. and Shoykhet, I. N., 2008: “Method to Eliminate Lost Returns and Build Integrity Continuously with High-Filtration-Rate Fluid.” Paper SPE 112656, presented in SPE/IADC Drilling Conference, Orlando, Florida, USA.

Fuh, G. F., Morita, N., Byod, P. A., and McGoffin, S. J. 1992: “A New Approach to Preventing Lost Circulation While Drilling.” Paper SPE 24599, presented at SPE Annual Technical Conference and Exhibition, Washington D.C., USA, 4-7 October.

Ghalambor A, S. Salehi, MP. Shahri and M. Karimi, 2014: “Integrated Workflow for Lost Circulation Prediction,” Paper SPE 168123, presented at the SPE International Symposium and Exhibition on Formation Damage Control, Society of Petroleum Engineers, Lafayette, Louisiana, USA.

Goldman, A. J., Cox, R. G., & Brenner, H., 1967: “Slow viscous motion of a sphere parallel to a plane wall—I Motion through a quiescent fluid.” Chemical engineering science, 22(4), 637-651.

Howard, G. C., and Scott, P. P., 1951: “An Analysis and the Control of Lost Circulation.” Journal of Petroleum Technology, Vol. 3 (6), pp. 171-185.

Israelachvili, J. N., 2015: “Intermolecular and surface forces.” Academic press.

Jain B, MA. Khattak, AM. Mesa, S. Al Kalbani, A. Meyer, S. Aghbari, A. Al-Salti, B. Hennette, M. Khaldi, A. Al-Yaqoubi and H. Al-Sharji, 2013: “Successful Implementation of Engineered Fiber Based Loss Circulation Control Solution to Effectively Cure Losses While Drilling, Cementing and Work Over Operations in Oman,” Paper SPE 166529, presented at the SPE Annual Technical Conference and Exhibition, Society of Petroleum Engineers, New Orleans, USA.

Kelsey, J. R., 1981: “Geothermal Drilling and Completion Technology Development Program Quarterly Progress Report.” SAND81-1020.

Kumar, A., and Savari, S. 2011: “Lost Circulation Control and Wellbore Strengthening: Looking Beyond Particle Size Distribution.” AADE-11 NTCE-21, AADE National Technical Conference and Exhibition, Houston, Texas, USA.

Lecolier, E., Herzhaft, B., Rousseau, L., Neau, L., Quillien, B., and Kieffer, J., 2005: “Development of a Nanocomposite Gel for Lost Circulation Treatment.” Paper SPE 94686, presented in SPE European Formation Damage Conference, Sheveningen. The Netherlands.

Lendlein, A., & Kelch, S. (2002): "Shape‐memory polymers." Angewandte Chemie International Edition, 41(12), 2034-2057.

Li, G. 2014: "Self-healing composites: shape memory polymer based structures."

Li, G., Ajisafe, O., and Meng, M., 2013: "Effect of strain hardening of shape memory polymer fibers on healing efficiency of thermosetting polymer composites."

Li, G., and Nettles, D., 2010: "Thermomechanical Characterization of a Shape Memory Polymer Based Self-Repairing Syntactic Foam." Polymer, 51(3), 755-762.

Li, G., and Xu, W., 2011: "Thermomechanical Behavior of Thermoset Shape Memory Polymer Programmed by Cold-Compression: Testing and Constitutive Modeling." Journal of the Mechanics and Physics of Solids, 59(6), 1231–1250.

Li, J and D J Mason. 2000: "A computational investigation of transient heat transfer in pneumatic transport of granular particles.pdf". In: pp. 273–282.

Liu, Y., Gall, K., Dunn, M. L., Greenberg, A. R., & Diani, J. 2006: "Thermomechanics of shape memory polymers: uniaxial experiments and constitutive modeling." *International Journal of Plasticity*, *22*(2), 279-313.

Mansour, A.K., Taleghani, A. D, and Li, G., 2017: "Smart Expandable LCMs; A Theoretical and Experimental Study." Paper AADE-17-NTCE-074, presented at the 2017 AADE National Technical Conference and Exhibition in Houston, Texas, USA.

Mansour, A.K., Taleghani, A. D., and Li, G., 2017: "Smart Lost Circulation Materials for Wellbore Strengthening." Paper ARMA 17-0492, presented at the 51st US Rock Mechanics/Geomechanics Symposium in San Francisco, California, USA.

Matsui H., M. Daitoh, K. Yoshimura and N. Morita, 2012: "Development of Environmentally Friendly Lost Circulation Materials for Riserless Drilling," Paper SPE 156575, presented in International Conference on Health, Safety and Environment in Oil and Gas Exploration and Production, Society of Petroleum Engineers, Perth, Australia.

Morita, N., Black, A. D., and Fuh, G-F., 1990: "Theory of Lost Circulation Pressure." Paper SPE 2040, presented inSPE Annual Technical Conference and Exhibition, New Orleans, Louisiana, USA.

Mostafavi, V., Hareland, G., Belayneh, M. and Aadnoy, B. S., 2011: "Experimental and Mechanistic Modeling of Fracture Sealing Resistance with Respect to Fluid and Fracture Properties." ARMA 11-98, the 45th US Rock Mechanics Symposium, San Francisco, USA.

Nygaard, R., Alsaba, M. & Hareland, G., 2014: "Review of Lost Circulation Materials and Treatments with an Updated Classification." Presented in AADE National Technical Conference and Exhibition, Houston, TX, USA.

O'Sullivan, Catherine. 2011: "Particulate discrete element modelling: a geomechanics perspective", p. 574. isbn: 9780415343046.

Peng, S. and Zhang, J., 2007: "Engineering geology for underground rocks." Springer Science & Business Media.

Ratna, D. and Karger-Kocsis, J., 2008: "Recent advances in shape memory polymers and composites: a review." Journal of Materials Science, 43, 254–269.

Rhodes, M. J., 2008: "Introduction to particle technology." John Wiley & Sons.

Salehi, S. 2012: "Numerical Simulations of Fracture Propagation and Sealing: Implication for Wellbore Strengthening." PhD dissertation, Department of Geological Sciences and Engineering, Missouri University of Science and Technology. USA.

Salehi, S. and Nygaard, R., 2012: "Numerical Modeling of Induced Fracture Propagation: A Novel Approach for Lost Circulation Materials (LCM) Design in Borehole Strengthening Applications of Deep Offshore Drilling." Paper SPE 135155, presented in SPE Annual Technical Conference and Exhibition, San Antonio, USA.

Sanders, M. W., J.T. Scorsone and J.E. Friedheim, 2010: "High-Fluid-Loss, High-Strength Lost Circulation Treatments," Paper SPE 135472, presented in SPE Deepwater Drilling and Completions Conference, Society of Petroleum Engineers, Galveston, Texas, USA.

Santos, L.,2016: "Smart Expandable Proppants to Achieve Sustainable Hydraulic Fracturing Treatments," Paper SPE 181391-MS presented in SPE Annual Technical Conference & Exhibition in Dubai, UAE.

Santos, L., A. Dahi Taleghani, Li, G., 2016: "Expandable Proppants For Hydrauilic Fracturing" Thesis Paper, Louisiana State University.

Santos, L., A. Dahi Taleghani, Li, G., 2017: "Expandable Diverting Agents to Improve Efficiency of Refracturing Treatments" Paper-URTeC 2697493, presented in the Oral presentation at the Unconventional Resources Technology Conference in Austin, Texas, USA.

Savari, S., D. L. Whiftill, D.E. Jamison and A.Kumar, 2014: "A Method To Evaluate Lost-Circulation Materials-Investigation of Effective Wellbore-Strengthening Applications," Paper SPE 167977, presented in SPE Drilling Conference and Exhibition, Society of Petroleum Engineers, Fort Worth, Texas, USA.

Savari, S., Kumar, A., Whitfill, D. L., Miller, M., Murphy, R. J., and Dale E. Jamison, 2013: "Engineered LCM Design Yields Novel Activating Material for Potential Application in Severe Lost Circulation Scenarios." Paper SPE 164748, presented in SPE North Africa Technical Conference and Exhibition, Cairo, Egypt.

Seville, J., Tüzün, U., & Clift, R., 2012: "Processing of particulate solids" (Vol. 9). Springer Science & Business Media.

Siskind, R. D., & Smith, R. C., 2008: "Model development for shape memory polymers." In The 15th International Symposium on: Smart Structures and Materials & Nondestructive Evaluation and Health Monitoring (pp. 69291H-69291H). International Society for Optics and Photonics.

Taleghani, A. D., Li, G., & Moayeri, M., 2016: "The Use of Temperature-Triggered Polymers to Seal Cement Voids and Fractures in Wells." SPE-PAPER-181384-MS Society of Petroleum Engineers.

Tsory, T., Ben-Jacob, N., Brosh, T., & Levy, A., 2013: "Thermal DEM–CFD modeling and simulation of heat transfer through packed bed." *Powder technology*, *244*, 52-60.

Van Oort, E., Friedheim, J., Pierce, T., and Lee, J., 2011: "Avoiding Losses in Depleted and Weak Zones by Constantly Strengthening Wellbores." Paper SPE 125093, presented in SPE Drilling & Completion, USA.

Vickers, S., Cowie, M., Jones, T., and Allan, J.T.: "A New Methodology that Surpasses Current Bridging Theories to Efficiently Seal a Varied Pore Throat Distribution as Found in Natural Reservoir Formations," paper AADE-06-DF-HO-16 presented at the 2006 AADE Fluids Conference held in Houston, Texas, USA, 11-12 April.

Wang H, Sweatman R, Engelman B, Deeg W, Whitfill D, Soliman M, Towler BF. 2008: "Best Practice in Understanding and Managing Lost Circulation Challenges." SPE Drilling & Completion, Vol. 23 (2), pp. 168-175.

Wang, A., & Li, G., 2015: "Stress memory of a thermoset shape memory polymer." *Journal of Applied Polymer Science*, *132*(24).

White, R. J., 1956: "Lost-circulation Materials and their Evaluation," In Drilling and Production Practice. American Petroleum Institute.

Whitfill, D., 2008: "Lost Circulation Material Selection, Particle Size Distribution and Fracture Modeling with Fracture Simulation Software." SPE-115039-MS, IADC/SPE Asia Pacific Drilling Technology Conference and Exhibition, Jakarta, Indonesia, 25- 27 August.

Whitfill, D. L. and H. Wang, 2005: "Making Economic Decisions To Mitigate Lost Circulation," Paper SPE 95561, presented in SPE Annual Technical Conference and Exhibition, Society of Petroleum Engineers, Dallas, Texas, USA.

Whitfill, D.L. and T. Hemphill, 2003: “All Lost-Circulation Materials and Systems Are Not Created Equal,” Paper SPE 84319, presented at the SPE Annual Technical Conference and Exhibition, Society of Petroleum Engineers, Denver, Colorado, USA.

Zhao, J., & Shan, T. 2013: “Coupled CFD–DEM simulation of fluid–particle interaction in geomechanics.” Powder technology, 239, 248-258.Zhu, H. P., Zhou, Z. Y., Yang, R. Y., & Yu, A. B., 2007: “Discrete particle simulation of particulate systems: theoretical developments.” *Chemical Engineering Science*, *62*(13), 3378-3396.

Appendix A: Permission To Use My Published Papers

Peter Smeallie <peterhsmeallie@gmail.com>

Hello Mr. Peter,

My name is Ahmed Mansour and i am a master thesis student at Louisiana State University. I have published an ARMA paper "ARMA 17-0492" in the national ARMA conference of 2017 in San Fransisco. I would like to include this paper in my final thesis report and would like to be granted permission to use my published paper for my final thesis report.

Thank you,
Ahmed Mansour

PS Peter Smeallie <peterhsmeallie@gmail.com>
Today, 7:49 AM

Dear Ahmed,

You have permission to use your paper from the ARMA meeting in your thesis with proper attribution.

Best,

Peter

Peter Smeallie
Executive Director
American Rock Mechanics Association
600 Woodland Terrace
Alexandria, VA 22302
703-683-1808 (office)
703-801-1088 (cell)
703-997-6112 (fax)
www.armarocks.org

Figure A1. Permission to use ARMA 17-0492 in my thesis

bvaughn2007@gmail.com

Hello Mr. Bob,
My name is Ahmed Mansour and i am a master thesis student at Louisiana State University. I have published an AADE paper "AADE-17-NTCE-074" in the national AADE conference of 2017. I would like to include this paper in my final thesis report and would like to be granted permission to use my published paper for my final thesis report.
Thank you,
Ahmed Mansour

BV

Bob Vaughn <bvaughn2007@gmail.com>
Today, 9:38 AM

Hi, Ahmed,

This is approved! Good luck with your thesis.

Bob

Bob Vaughn
Executive Director
American Association of Drilling Engineers (AADE)
bvaughn2007@gmail.com

1201 Canal St., Unit 653
New Orleans, LA 70112
(504) 899-7111 (home)
(832) 671-6700 (mobile)

Figure A2. Permission to use AADE-17-NTCE-074 in my thesis

Appendix B: Experimental Components

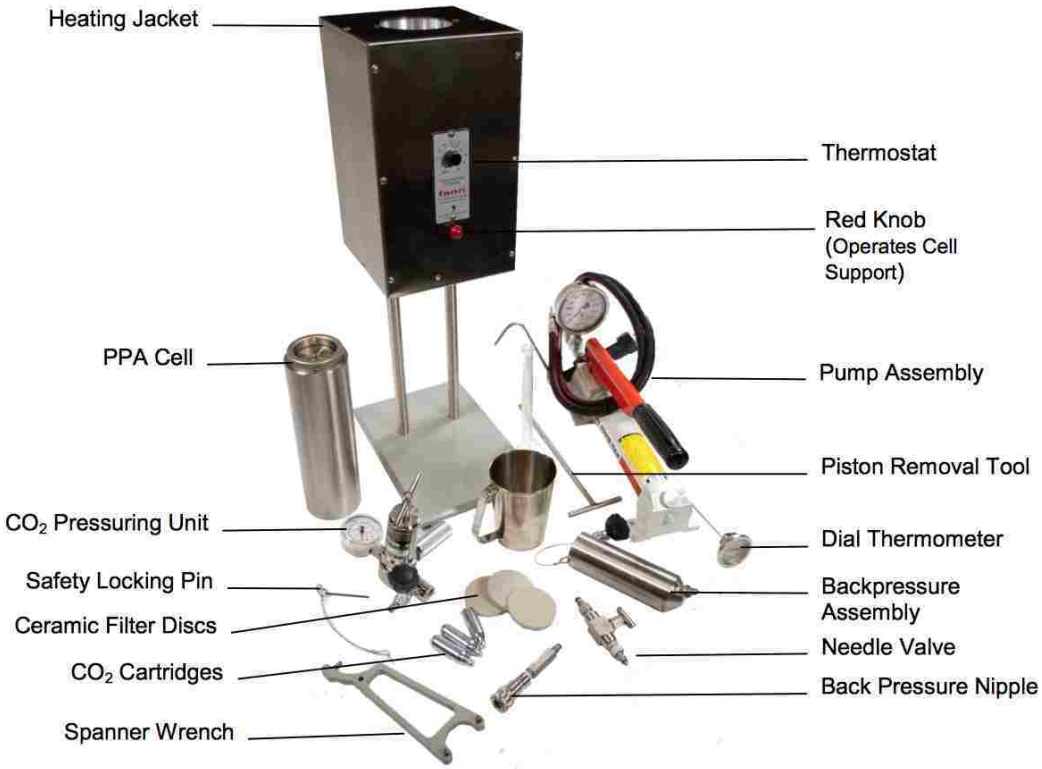

Figure B1- Permeability Plugging Apparatus

Figure B2- LCM Receiver that gets attached to the PPA cell instead of the backpressure receiver.

Vita

Ahmed Mansour was born in the year of 1993 in Kuwait. He is originally from Cairo, Egypt. He started studying petroleum engineering in the American University in Cairo and then transferred to Louisiana State University in 2012. He completed his undergraduate studies in Petroleum Engineering at Louisiana State University on May, 2015. During his years of education he had several internships in the oil and gas industry, where he trained as a drilling and a production engineer. He is a candidate to receive master's degree in December 2017 and plan to work in the oil and gas industry as a drilling engineer to gain experience. He then plans to pursue his doctoral degree in the topic area of wellbore strengthening or fracture mechanics.